



Universiteit
Leiden

The Netherlands

Photodynamic therapy-based combinations with immunotherapy in colon cancer treatment

Hao, Y.

Citation

Hao, Y. (2023, January 18). *Photodynamic therapy-based combinations with immunotherapy in colon cancer treatment*. Retrieved from <https://hdl.handle.net/1887/3511806>

Version: Publisher's Version

License: [Licence agreement concerning inclusion of doctoral thesis in the Institutional Repository of the University of Leiden](#)

Downloaded from: <https://hdl.handle.net/1887/3511806>

Note: To cite this publication please use the final published version (if applicable).



02

Combination of Photodynamic Therapy and Stimulator of Interferon Genes (STING) Agonist Inhibits Colorectal Tumor Growth and Recurrence

This chapter was adapted from “Hao, Y., Ma, S., Gu, Z., Haghparast, A., Schomann, T., Dong, X., He, Y., Cruz, L. J. & Ten Dijke, P. (2022). Cancer Communications (accepted) “

Abstract

Photodynamic therapy (PDT) is recognized as a promising approach for the treatment of cancer. With the advent of photoimmunotherapy, it is valuable to investigate the novel combination of PDT with different immunotherapy regimens for cancer treatment. In this study, we studied the anti-tumor effects of PDT in combination with an emerging immune therapy: the agonist of the stimulator of interferon genes (STING), and its potential immunological mechanisms in an immunocompetent syngeneic mouse model. The combination of PDT with the intratumoral application of ADU-S100 converted the tumor microenvironment (TME) and the tumor-draining lymph nodes (dLNs) from an immunosuppressive to a pro-inflammatory state. Additionally, PDT in combination with ADU-S100 increased the number of CD4⁺ helper and CD8⁺ cytotoxic T lymphocytes in the tumor thereby enhancing adaptive immune responses. Combinational therapy promoted immunological memory by increased infiltration of effector memory CD4⁺ and CD8⁺ T cell responses, resulting in a long-lasting and profound systemic immunity. These anti-tumor immunities induced by combination therapy in turn demonstrated the ability to effectively combat tumor recurrence and exhibit a distant compartmentalization effect.

Keywords: Photodynamic therapy; Cancer immunotherapy; cGAS-STING; Immune adjuvants; Therapeutic combined therapy; Tumor microenvironment

1. Introduction

Colorectal cancer (CRC) is the third most common cancer worldwide, accounting for about one in ten cancer-related deaths worldwide [1,2]. CRC is classified into different stages based on the histological characteristics of the tumor and the invasion of lymph nodes by tumor cells [3]. Early-stage CRC is considered an easily curable cancer with conventional surgery and adjuvant chemotherapy. For patients with advanced CRC, a combination of radiotherapy, radiofrequency ablation, targeted therapy, and immunotherapy for palliative treatment has been the mainstream treatment in anticipation of prolonging patient survival and reducing the pain and cost of treatment [4].

Photodynamic therapy (PDT), as a clinically approved and promising treatment modality with the advantage of low toxicity to healthy tissues, has shown a promising potential in the treatment of CRC [5,6]. The mechanism of PDT is that the photosensitizer (PS) can be activated by the corresponding wavelength of excitation light in the presence of oxygen to produce reactive oxygen species (ROS) capable of causing intracellular oxidative stress and triggering tumor cell death [7]. In addition, it has been shown that PDT-induced vascular rupture and acute inflammation [8- 10], thereby leading to a series of immune responses, such as dendritic cells (DCs) activation, neutrophil infiltration, and T-cell immunity [11,12]. Although great progress has been made in the clinical use of PDT for the treatment of patients with superficial tumors. However, cancer recurrence and metastasis have limited the application of PDT in the treatment of solid tumors and advanced cancers [13,14,15]. The way to improve PDT efficiency in the field of cancer treatment could be developing new photosensitizers with better physicochemical properties, optimizing the irradiation laser for PDT, and overcoming the oxygen supplement during treatment procedure. For example, Woo Seok Kim and colleagues recently developed a biocompatible, miniaturized, implantable LED device that improves PDT for CRC treatment by real-time monitoring of the tumor response and immediate adjustment of the light dose [16].

In this context, combining PDT with other complementary immunotherapy regimens [17,18] may overcome these limitations of PDT. Previous combination therapies for PDT have focused on immune checkpoint blockade, conventional vaccines, immunoadjuvants, T-cell activators, and nonspecific immune therapies [19]. In recent years, new strategies targeting the stimulator of interferon genes (STING) protein, which is the main innate immune pathway involved in spontaneous anti-tumor T-cell responses, have been promising to further advance the development of cancer immunotherapy [20]. Since 2012, when small molecule drug 5,6-dimethylxanthenone-4-acetic acid (DMXAA) was shown to have tumor controllable effects in mice via activation of the STING pathway [21], STING agonist-triggered anti-tumor immunity has been extensively studied and has been shown to be intratumorally injectable to enhance anti-tumor immune responses by modulating each phase of the cancer immune cycle [20]. Now, STING agonists have entered clinical development, such as cyclic dinucleotides (CDN), including cyclic dimeric guanosine monophosphate (c-di-GMP), cyclic di-adenosine monophosphate (c-di-AMP), cyclic guanosine monophosphate (c-GMP), etc. [22]. Among them, ADU-S100 is a safe and potent synthetic CDN. Phase II trials investigating the combination of ADU-S100 with programmed cell death protein 1 (PD-1) antibody for head and neck cancer and ADU-S100 with Ipilimumab (targeting CTLA-4) for the treatment of patients with advanced solid tumors or lymphomas have been completed [22,23]. The rationale for developing the combination of PDT and STING agonist immunotherapy (ADU-S100) is based on studies showing that intratumoral administration of STING agonist stimulates cross-presentation of tumor antigens and T-cell mediated activation of DCs to drive the production of type I interferon (IFN) and other cytokines, thereby curing cancer or delaying tumor progression [24]. Notably, activation of the STING signaling pathway also converts macrophages from an immunosuppressive M2-like phenotype to M1-like phenotype that facilitates cancer therapy [25,26]. It has also been shown to cause specific

vascular disruption one day after intratumoral injection and to promote vascular normalization in the TME within one week, which has been proved to increase T-cell infiltration and the recovery of T cell function [26,27,28,29]. However, to our knowledge, preclinical studies on the efficiency and potential mechanism of action of the combination therapy (PDT+ADU-S100) in mouse models have not been performed so far. Therefore, considering that PDT and ADU-S100 act in different but partially overlapping ways, the combination of PDT with STING agonists may be a new and safe combination therapy for the effective treatment of colon tumors.

Here, we aimed to elucidate the inhibitory efficiency of PDT in combination with an agonist stimulator of interferon genes (STING) in colorectal cancer (CRC) models and to explore the underlying regulatory effects on the host immune system. We explored the biological effects of PDT and ADU-S100 *in vitro*, specifically investigating the effect of the combination treatment on the activation of immature DCs and on the polarization of bone marrow-derived macrophages (BMDMs) and investigated the anti-tumor activity of the combination therapy *in vivo* using two murine CRC models. This study also explores the unique imaging capabilities of the photosensitizer Verteporfin. And we study the alterations in the TME, and activation of systemic immunity after our combination therapy. In addition, we investigated the potential of combination therapy against tumor recurrence by cancer cells rechallenge and immune memory cell type identification. Finally, the potential of PDT in combination with ADU-S100 in metastasized CRC treatment efficacy has been explored in a bilateral-tumor mouse model.

2. Materials and methods

2.1. Cell lines and cell culture

Murine MC38 and CT26 colon carcinoma cell lines were grown in full Iscove's modified Dulbecco's medium (IMDM; Lonza, Basel, Switzerland) supplemented with 10% heat-inactivated fetal calf serum (FCS; Sigma–Aldrich, St. Louis, MO, USA), 2 mM l-glutamine (Gibco, Paisley, UK), 25 mmol/L 2-mercaptoethanol (Sigma–Aldrich, St. Louis, MO, USA), and 100 IU/mL penicillin–streptomycin (Gibco, Paisley, UK) in a CO₂ incubator (Panasonic, Kadoma, Japan). We confirmed that there was an absence of species-specific viruses and mycoplasma in the cell lines that were used in this study.

2.2. Animals

Immunocompetent female C57BL/6 and BALB/c mice were provided by a company (ENVIGO, Horst, the Netherlands) and housed in pathogen-free animal facilities at Leiden University Medical Center (LUMC; Leiden, the Netherlands). All the experimental animals were 8-12 weeks old unless otherwise stated. The animal experiments were designed according to the guidelines of the Dutch Animal Ethics Committee's Code of Conduct, with a project license AVD116008045, and approved by the Animal Experimentation Committee of LUMC.

2.3. *In vivo* tumor models

To determine the effect of the combination treatment on primary tumors, 4×10^5 MC38 or 1×10^5 CT26 mouse CRC tumor cells in 100 μ L phosphate-buffered saline (PBS) were subcutaneously injected into the right flanks of C57BL/6 or BALB/c female mice. Approximately one week after injection, the mice had established tumors (75-125 mm³), and according to the experimental design, they were randomly divided into different treatment groups: the Control (PBS), PDT, ADU-S100, and PDT in combination with ADU-S100 (PDT+ADU-S100) groups. PDT treatment was performed using a standard protocol. Before irradiation, the skin surrounding the tumor area of the tumor-bearing mice was shaved while the mice were under isoflurane anesthesia and on a heat mat [30]. The mice were first administered 0.15 mg/kg verteporfin (VP; MedChemExpress, Princeton, NJ, USA) solution by a slow intravenous (i.v.) injection over 4-6 min and then received 690 nm laser irradiation at a fluence rate of 200 mW/cm² for a total fluence of 100 J/cm². ADU-S100 treatment was carried out by intratumoural injection of 50 μ g ADU-S100 in a total volume of 30 μ L per treatment. The mice were monitored regularly during the experimental observation period, and tumor growth (with calipers) and weight were measured. The tumor volume was calculated using the formula (L*W*H). Additionally, the survival of the mice was monitored, and the mice were euthanized according to the humane endpoints established in the code of practice for cancer research, including MC38 tumor size over 1500 mm³ and CT26 tumor size over 1000 mm³; body weight loss of 15% or more compared to the previous measurement; body weight loss of more than 20% compared to starting weight; and other signs of distress.

To determine the immune memory of the mice subjected to an MC38 or CT26 single tumor challenge but that were tumor-free after our treatments, the mice were reinoculated with 4×10^5 MC38 cells or 1×10^5 CT26 cells in 100 μ L PBS in their left flanks. Age-matched

naïve female mice ($n = 5$) were used as controls and injected with the same number of tumor cells. Tumor size was measured as described above. At 21 days after the rechallenge, the blood, spleen, and lymph nodes were harvested for flow cytometry analysis.

To determine the abscopal effect of combination treatment on distant tumors, 4×10^5 MC38 or 1×10^5 CT26 mouse CRC tumor cells in 100 μ L PBS were subcutaneously injected into the right flanks of C57BL/6 or BALB/c female mice at day 0, and the left flanks received a secondary injection at day 3 to mimic small metastatic tumors. When the initially inoculated tumors reached the established tumor volume (75-125 mm³), the mice were randomized into the same treatment groups as described for the previous single tumor model and received the corresponding treatments. The tumors in both the treated and untreated mice were measured with calipers to assess tumor growth, and the welfare of the mice was monitored until the end of the experiment.

2.4. Flow cytometry

To analyze the uptake, binding, and retention of the photosensitizer VP in colon tumor cell lines *in vitro*, 7-10 $\times 10^3$ MC38 or CT26 cells were seeded in 96-well plates (Greiner, Alphen aan den Rijn, the Netherlands) and allowed to attach overnight. For the uptake experiments, the cells were incubated with VP (0.5 μ mol/L) at 37°C for 1, 3 or 6 h. The cells were then washed 3 times in PBS and fixed immediately in PBS supplemented with 1% formalin (Sigma–Aldrich, St. Louis, MO, USA) at 4°C for 15 min. After fixation, the collected cells were washed in PBS and resuspended in FACS buffer (PBS with 0.5% BSA and 0.02% sodium azide) before analysis by an LSR II flow cytometer (BD Biosciences). For the binding experiments, cells were prechilled at 4°C for 4 h before incubation with VP (0.5 μ mol/L). The cells were then collected using the same procedure as in the uptake experiment for flow cytometry analysis. For the retention experiment, cells were incubated with VP (0.5 μ mol/L) for 3 h were washed 3 times in PBS, and then, VP-free medium was added. After 0, 1, and 3 h, the cells were collected for flow cytometric analysis following the same protocol as described for the uptake assay. The geometric mean fluorescence intensity (gMFI) of the cells was then measured by an LSR II flow cytometer (BD Biosciences, Franklin Lakes, NJ, USA).

To assess the apoptosis induced by *in vitro* PDT using VP (VP-PDT) in colon tumor cell lines, 3-5 $\times 10^4$ MC38 or CT26 cells were seeded in a 24-well plate (Corning, New York, USA) and allowed to attach overnight. The next day, the cells were incubated with VP (0.003-1 μ mol/L) for 3 h, washed 3 times in PBS, and given fresh medium. Illumination was performed using a 690 nm laser at a fluence rate of 200 mW/cm² for a total light fluence of 25 J/cm². The next day, the cells were stained with Annexin V-FITC (Invitrogen, Waltham, MA, USA) and 0.25 μ mol/L 4',6-diamidino-2-phenylindole (DAPI; Sigma–Aldrich) in annexin V binding buffer (0.1 mol/L HEPES, 1.4 mol/L NaCl, and 25 mmol/L CaCl₂ in deionized water with pH 7.4, sterile filtered using a 0.2 μ m filter) at room temperature for 20 min before analysis with an LSR II flow cytometer.

To measure the ROS levels that were induced by *in vitro* PDT using VP (VP-PDT) in colon tumor cell lines, 3-5 $\times 10^4$ MC38 or CT26 cells were seeded in a 24-well plate and allowed to attach overnight. The next day, the cells were incubated with VP (0.003-1 μ mol/L) for 3

h, washed 3 times in PBS, and given fresh medium. Illumination was performed using a 690 nm laser at a fluence rate of 200 mW/cm² for a total light fluence of 25 J/cm². After PDT, the cells were collected and stained with 10 μmol/L 2',7'-dichlorodihydrofluorescein diacetate (DCFH-DA) (Abcam, Catalog#ab113851, USA) for 30 min before analysis with an LSR-II flow cytometer.

To analyze the phagocytosis of PDT-treated tumor cells by D1DCs (immature murine DCs D1 [31]) *in vitro*, we used 5-chloromethylfluorescein diacetate (CMFDA; Abcam, Cambridge, UK), which is a fluorescent dye, to monitor tumor cell movement. Untreated tumor cells or those treated with standard *in vitro* PDT were added to immature DCs immediately after PDT at a ratio of 1:1 or 1:5 and cocultured for 2 h. Then, the harvested cells were stained with anti-CD11c-APC-eF780 (clone N418, Thermo Fisher) for LSR-II flow cytometric analysis. CD11c⁺ and CMFDA⁺ double-positive DCs were considered to be DCs that phagocytosed tumor cells.

To detect the DC activation induced by PDT-treated tumor cells and/or ADU-S100 *in vitro*, 5 × 10⁴ DCs were cocultured with either MC38 tumor cells undergoing PDT-induced cell death or MC38 tumor cells undergoing cell death induced by 3 freeze/thaw (F/T) cycles at -20°C at a ratio of 1:5 for 24 h, with or without 20 ng/mL ADU-S100. The cells were collected and stained with the following antibodies and DAPI to assess DC activation: anti-CD11c-APC-eF780 (Clone N418, Thermo Fisher, USA), anti-CD40-APC (Clone 3/23, Biolegend, San Diego, CA, USA), anti-CD86-PE-cy7 (clone GL1, BD Biosciences, USA), and anti-I-Ab-PE (major histocompatibility complex (MHC) class II; Clone M5/114.15.2, Thermo Fisher, Waltham, MA, USA). Analysis was performed using an LSR-II flow cytometer.

To detect the effects of ADU-S100 on the repolarization of M2-type macrophages *in vitro*, bone marrow cells were collected from mice and then differentiated into BMDMs (M0 phenotype) following an established protocol [32]. The purity of the population was examined before the experiment by staining with anti-CD11b-FITC (clone M1/70, BD Biosciences) and anti-F4/80-PE-cy5 (clone BM8, Thermo Fisher). Next, 2.5×10⁴ BMDMs were cultured with 500 ng/mL lipopolysaccharide (LPS) and 25 ng/mL interferon (IFN)-γ to induce their polarization toward the M1 phenotype or 20 ng/mL interleukin (IL)-4 to induce their polarization toward the M2 phenotype. The next day, M2-type cells were treated with 25 μg/mL ADU-S100 for another 24 h and then harvested and stained with antibodies for LSR-II flow cytometer analysis. The antibodies used for this experiment were anti-CD86-FITC (clone GL1, Thermo Fisher), anti-I-A/I-E-V500 (MHC class II; clone M5/114.15.2, BD Biosciences), anti-CD206-biotin (clone C068C2, Biolegend), and Streptavidin-PerCP (Biolegend).

To detect the distribution of immune cells in the blood, tumors, and secondary immune organs, single-cell suspensions were generated as described before and stained with multiplexed monoclonal antibodies [33]. The antibodies used to stain the lymphoid population were anti-CD45.2-APC-ef780 (clone 104, Thermo Fisher), anti-CD3-BV421 (clone 17A2, Biolegend), anti-CD4-Brilliant Violet 605 (clone RM4-5, Biolegend), and anti-CD8α-APC-R700 (clone 53-6.7, BD Bioscience). Anti-IFN-γ-PE-cy7 (clone B27, Biolegend) and anti-tumor necrosis factor (TNF)-α-BV785 (clone MP6-XT22, Biolegend) were used

for intracellular staining according to the manufacturer's instructions. To assess changes in the myeloid cell population in dLNs, the following antibodies were used: anti-CD45.2-PerCP-Cy5.5 (clone 104, BD Biosciences), anti-CD11b-ef450 (clone M1/70, BD Biosciences), anti-Ly6G-BV785 (clone 1A8, Biolegend), anti-Ly6C-BV605 (clone HK1.4, Biolegend), anti-CD11c-APC-ef780 (clone HL3, Thermo Fisher), anti-CD40-PE (clone 3/23, BD Biosciences), and anti-CD86-APC (clone GL1, Thermo Fisher). Additionally, B-cell activation was assessed by staining with anti-CD45.2-APC-ef780, anti-CD3-BV421, anti-CD19-BV655 (clone 6D5, Thermo Fisher), anti-CD40-APC, and anti-CD86-FITC (clone GL1, Thermo Fisher). Analysis was performed using an Aurora cytometer (Cytex Biosciences B.V., Amsterdam, the Netherlands).

To assess immune memory in tumor-challenged but tumor-free mice after treatment, the anti-CD45.2-APC-ef780, anti-CD3-BV421, anti-CD4-Brilliant Violet 605, anti-CD8 α -APC-R700, anti-CD44-PE (clone IM7, Thermo Fisher), and anti-CD62L-APC (clone MEL-14, Thermo Fisher) antibodies were used. Analysis was performed using an Aurora cytometer.

2.5. Near-infrared (NIR) signal measurements

To detect the NIR signal of VP in vitro, $7-10 \times 10^3$ MC38 or CT26 cells were seeded in 96-well black plates (ThermoFisher) and allowed to attach overnight. The next day, the tumor cells were incubated with VP (0.003-1 $\mu\text{mol/L}$) for 3 h, washed 3 times in PBS, and given fresh medium. The signal intensity of each well was measured at 700 nm on a SpectraMax ID3 microplate reader (Molecular Devices, San Jose, CA, USA) to evaluate the cellular uptake of VP.

2.6. Killing assay (MTS assay)

To detect the effect of VP on the viability of colon tumor cell lines with and without laser excitation, $7-10 \times 10^3$ MC38 or CT26 cells were seeded into the 96-well black plates and allowed to attach overnight. The next day, the tumor cells were incubated with VP (0.003-1 $\mu\text{mol/L}$) for 3 h, washed 3 times in PBS, and supplied with a fresh medium. Illumination was performed using a 690 nm laser at the fluence rate of 200 mW/cm² for a total light fluence of 25 J/cm². Next, 20 μL MTS reagent (CellTiter 96[®] Aqueous One, #G3581, Promega) was added to each well 24 h post-irradiation and incubated for 1-4 h at 37°C. To measure the background signal, wells containing only medium were included. The optical density (OD) value of each well was measured at 490 nm using a spectrum analyzer (Biolegend, Bio-Rad, iMark set). Cell viability is expressed in percentage (%) and calculated using the following formula: $(\text{OD } 490 \text{ nm treated cells} - \text{OD } 490 \text{ nm background}) / (\text{OD } 490 \text{ nm untreated cells} - \text{OD } 490 \text{ nm background}) \times 100$.

2.7. Intracellular fluorescence staining

To analyze the intracellular uptake of VP by colon tumor cell lines, $1.5-2.5 \times 10^4$ MC38 or CT26 cells were seeded in a 24-well plate containing coverslips and allowed to attach overnight. The next day, tumor cells were incubated with VP for 3 h, washed 3 times in PBS and fixed in PBS supplemented with 1% formalin at room temperature for 15 min. After the formalin was removed, the cells were washed and stained with 50 $\mu\text{g/mL}$ anti-CD44-FITC (clone IM7, Thermo Fisher) at 4°C for 30 min, washed 3 times in PBS, and

stained with 0.25 $\mu\text{mol/L}$ DAPI at room temperature for 5 min. After being washed, the coverslips were mounted on glass slides using Mowiol mounting medium (Sigma-Aldrich) and sealed with nail polish. Images were captured using a Leica DM 5000B fluorescence microscope.

To visualize M2-type macrophage repolarization *in vitro*, 1.5×10^5 BMDMs were seeded in a 24-well plate containing coverslips and allowed to attach overnight. The next day, 500 ng/mL LPS and 25 ng/mL interferon (IFN)- γ were added to the medium and incubated for 24 h to induce polarization toward the M1 phenotype or 20 ng/mL IL-4 to induce polarization toward the M2 phenotype. Then, M2 cells were treated for 24 h with 25 $\mu\text{g/mL}$ ADU-S100. The next day, BMDMs were washed 3 times in PBS, fixed, permeabilized, blocked and then stained with DAPI, anti-CD206-AF647 (clone C068C2, Biolegend), and anti-iNOS-FITC (clone RUO, BD Biosciences) for imaging using a Leica SP8 confocal microscope.

2.8. Primers and real-time quantitative reverse transcription polymerase chain reaction (qRT-PCR)

Treated tumors in all the subgroups were collected 3 h after the first treatment with ADU-S100. Total tumor RNA (3 mice per group) was extracted from TRIzol (Thermo Fisher)-preserved tumor lysates using isopropanol (Sigma-Aldrich) precipitation. Complementary DNA synthesis was performed with 1 μg of RNA using a RevertAid First Strand cDNA Synthesis Kit (ThermoFisher), and qRT-PCR was conducted with SYBR Green (Promega, Madison, WI, USA) in a CFX Connect Detection System (Bio-Rad Laboratories, Hercules, CA, USA). The thermal cycling used here are as shown following steps: initial 95°C for 10 minutes, followed by 40 cycles of denaturation at 95°C for 15 seconds, annealing at 60°C for 1 minute. The gene expression data were analyzed, and GAPDH was used as the housekeeping gene. The murine forward and reverse primers used to measure the expression of inflammatory genes are shown as follows: mouse IFN- γ : Forward, 5'-CCTTCTTCAGCAACAGCAAGGCG-3'; Reverse, 5'-CCCACCCCGAATCAGCAGCG-3'; mouse interleukin (IL)-6: Forward, 5'-AGACAAAGCCAAGT CCTTCAGAGA-3'; Reverse, 5'-GCCACTCCTTCTGTGACTCCAGC-3'; mouse tumor necrosis factor (TNF)- α : Forward, 5'-TCGTAGCAAACCACCAAGTG-3'; Reverse, 5'-GGAGTAGACAAGGTACAACC-3'; mouse Nitric Oxide Synthase (NOS) 2: Forward, 5'-TGCATGGACCAGTATAAGGCAAGC-3'; Reverse, 5'-GCTTCTGGTCGATGTCATGAGCAA-3'; mouse C-X-C Motif Chemokine Ligand (CXCL) 9: Forward, 5'-CCTAGTGATAAGGAATGCACGATG-3'; Reverse, 5'-CTAGGCAGGTTTGTATCTCCGTTT-3'; mouse C-X-C Motif Chemokine Ligand (CXCL) 10: Forward, 5'-ATCATCCCTGCGAGCCTATCCT-3'; Reverse, 5'-GACCTTTTTTGGCTAAACGCTTTC-3'; mouse Arginase 1 (ARG1): Forward, 5'-CAGAAGAATGGAAGAGTCAG-3'; Reverse, 5'-CAGATATGCAGGGAGTCACC-3'; mouse Glyceraldehyde 3-phosphate dehydrogenase (GAPDH): Forward, 5'-TGGCAAAGTGGAGATTGTTGCC-3'; Reverse, 5'-AAGATGGTGATGGGCTTCCCG-3'.

2.9. Histology of tumors

Tumor tissues from untreated control and treated subgroups were harvested on day 10, and then, dehydration, embedding, and preparation of paraffin sections at 5 μm thickness were performed. The standard immunohistochemical protocol was followed to stain the tumor sections. Briefly, the sections were dewaxed, hydrated, and stained with hematoxylin and eosin (H&E) to visualize morphology.

In the Ki67 immunohistochemistry experiments, paraffin-embedded sections were first dewaxed and rehydrated, boiled in Tris-EDTA (pH 9.0) buffer for 10 min, and then cooled at room temperature for 30 min for antigen repair. The sections were then incubated with a 3% H_2O_2 solution to inactivate endogenous peroxidase and in a blocking solution (PBS + 5% BSA) for 30 min. Subsequently, primary antibodies against Ki67 were added dropwise and incubated overnight at 4°C, followed by HRP-conjugated secondary antibodies. The DAB peroxidase substrate was used for visualization, hematoxylin was used for restraining, and the stained tissue sections were finally dehydrated, cleared, and blocked.

2.10. Enzyme-linked immunosorbent assay (ELISA)

Purified anti-mouse IL-12/IL-23 p40 (clone C15.6, Biolegend) and biotin-labeled anti-mouse IL-12/IL-23 p40 antibodies (clone C17.8, Biolegend) were used to measure the IL-12 levels in the cell supernatants by standard sandwich ELISA. Streptavidin-horseradish peroxidase (Biolegend) and 3,3',5,5'-tetramethylbenzidine (Sigma-Aldrich, USA) were used to generate the signal. Finally, the plates were read at 450 nm using a Bio-Rad 680 ELISA instrument (Bio-Rad Laboratories B.V.).

To analyze the total immunoglobulin G (IgG) levels in the serum of treated mice, we collected 50 μL caudal vein blood from MC38 tumor-bearing mice 23 days post tumor inoculation and allowed the blood to clot by leaving it undisturbed at room temperature for 30-60 min. Then, the blood was centrifuged at 1,000-2,000 $\times g$ for 10 min, and the supernatant was collected and stored at -80 °C for further analysis using the IgG (total) Mouse Uncoated ELISA Kit (Invitrogen, USA).

2.11. Ex vivo IVIS optical imaging and photoacoustic (PA) imaging

Ex vivo analysis was performed with CT26 tumor-bearing mice 10 days postinoculation (1×10^5 CT26 cells in 100 μL PBS were injected subcutaneously). After the administration of 0.15 mg/kg VP solution by slow i.v. injection, one mouse was sacrificed and its organs were collected for *ex vivo* analysis at each indicated time point (0, 1, 3, 6, 12, and 24 h). After optimization, we chose the time point that showed the highest fluorescence signal to perform the optical imaging again with tumor-bearing mice ($n = 3$).

The photoacoustic (PA) and B-mode ultrasound images were obtained under isoflurane anesthesia by LAZR-X (FUJIFILM VisualSonics, Tokyo, Japan) 15 min post-VP injection. For this measurement, an MX550D transducer was used with a center transmit of 40 MHz and an axial resolution of 40 μm . PA spectra were obtained over a cross-section of the tumor at 690 nm.

The data were analyzed using Living Image IVIS software (PerkinElmer, Waltham, Massachusetts, USA) and Vevo LAB v5.5.0 (FUJIFILM), respectively.

2.12. Statistical analysis

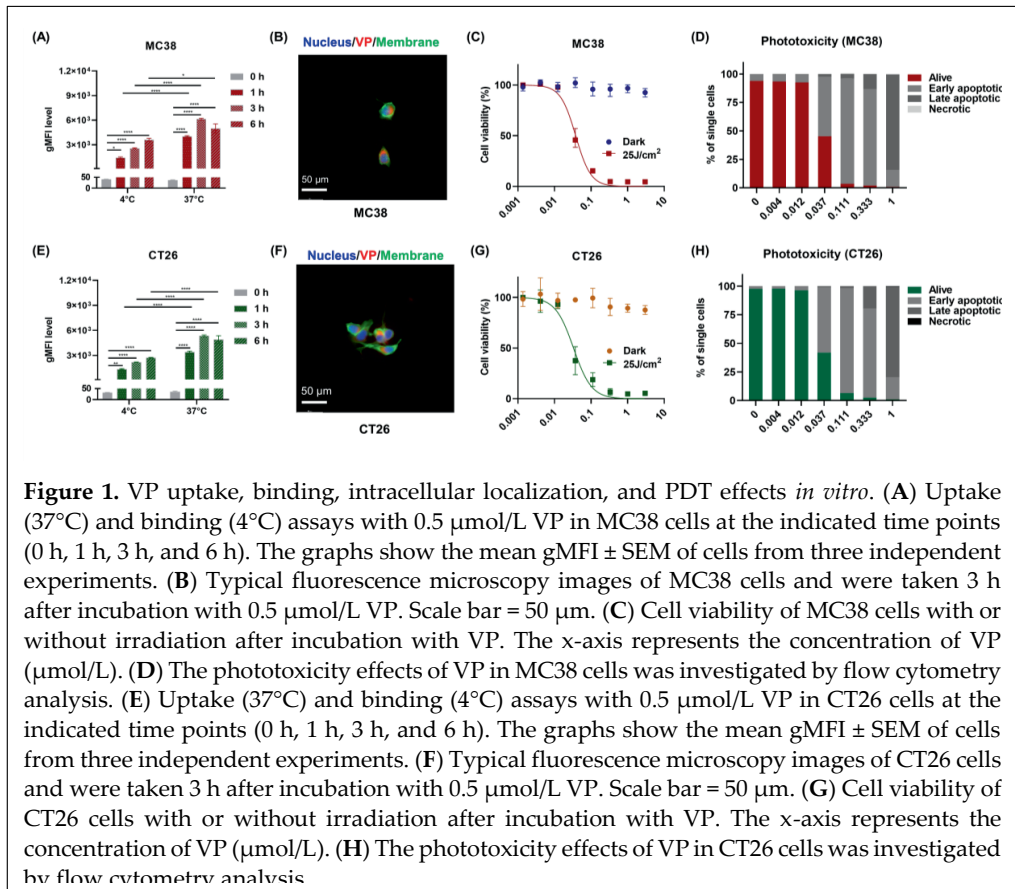
All the data were analyzed using GraphPad Prism software version 9.0 (La Jolla, CA, USA). Unless otherwise stated, the data are shown as the mean \pm standard error (SEM) of three independent experiments and were statistically analyzed by an unpaired two-tailed Student's *t* test or one-way analysis of variance (ANOVA). Statistical differences were considered significant at * $p < 0.05$, ** $p < 0.01$, *** $p < 0.001$, and **** $p < 0.0001$.

3 Results

3.1. VP intracellular uptake and mediated PDT effects *in vitro*

First, we characterized the binding and uptake kinetics of VP *in two* CRC cell lines. After incubation with 0.5 $\mu\text{mol/L}$ VP, fluorescent signals were detected in MC38 tumor cells at all time points and two temperatures. At 4°C, the fluorescence signal increased with extending incubation time. However, at 37°C, the fluorescence intensity peaked at 3 h of incubation and a significant increase in signal was observed at each time point compared to 4°C (Figure 1A). Moreover, by detecting the intracellular NIR signal (700 nm), we also confirmed the uptake of VP by tumor cells *in vitro*. This increase in fluorescence intensity was dose-dependent (Supplementary Fig.1A, B). We subsequently observed strong fluorescence signals in the cytoplasm of MC38 cells (Figure 1B) in the fluorescence images, indicating that VP was internalized into tumor cells after incubation and could be detected at least within 3 h (Supplementary Fig.1C). Further, we analyzed the effect of VP on the viability of CRC cells in the presence or absence of light. When MC38 cells were incubated in the dark with concentrations up to 3 $\mu\text{mol/L}$ of VP, no significant effects on cell viability were observed in the cell line (Figure 1C). However, when exposed to light with the appropriate wavelength (690 nm), VP exhibited significant toxicity to tumor cells by ROS generation with a half maximal inhibitory concentration (IC₅₀) of 30-40 nmol/L (Figure 1C, Supplementary Fig.1D). Subsequently, PDT-treated cells were analyzed for apoptosis and, in agreement with our MTS assay results, we observed approximately 50 % death (including early apoptotic, late apoptotic, and necrotic cells) of MC38 cells at a VP concentration of 37 nmol/L. VP-based PDT induced complete cell death in MC38 when the VP concentration was higher than 100 nmol/L (Figure 1D). In addition, we investigated the effect of time intervals between VP injection and laser irradiation on the killing effect of PDT. The results showed that tumor cells, which were subjected to laser irradiation immediately (0 h) after initial incubation with 0.5 $\mu\text{mol/L}$ VP, showed the highest sensitivity to PDT. Interestingly, VP-PDT had almost no effect when the intervals was 3 h between VP injection and laser irradiation, which corresponded with a decrease in intracellular VP (Supplementary Fig.1E).

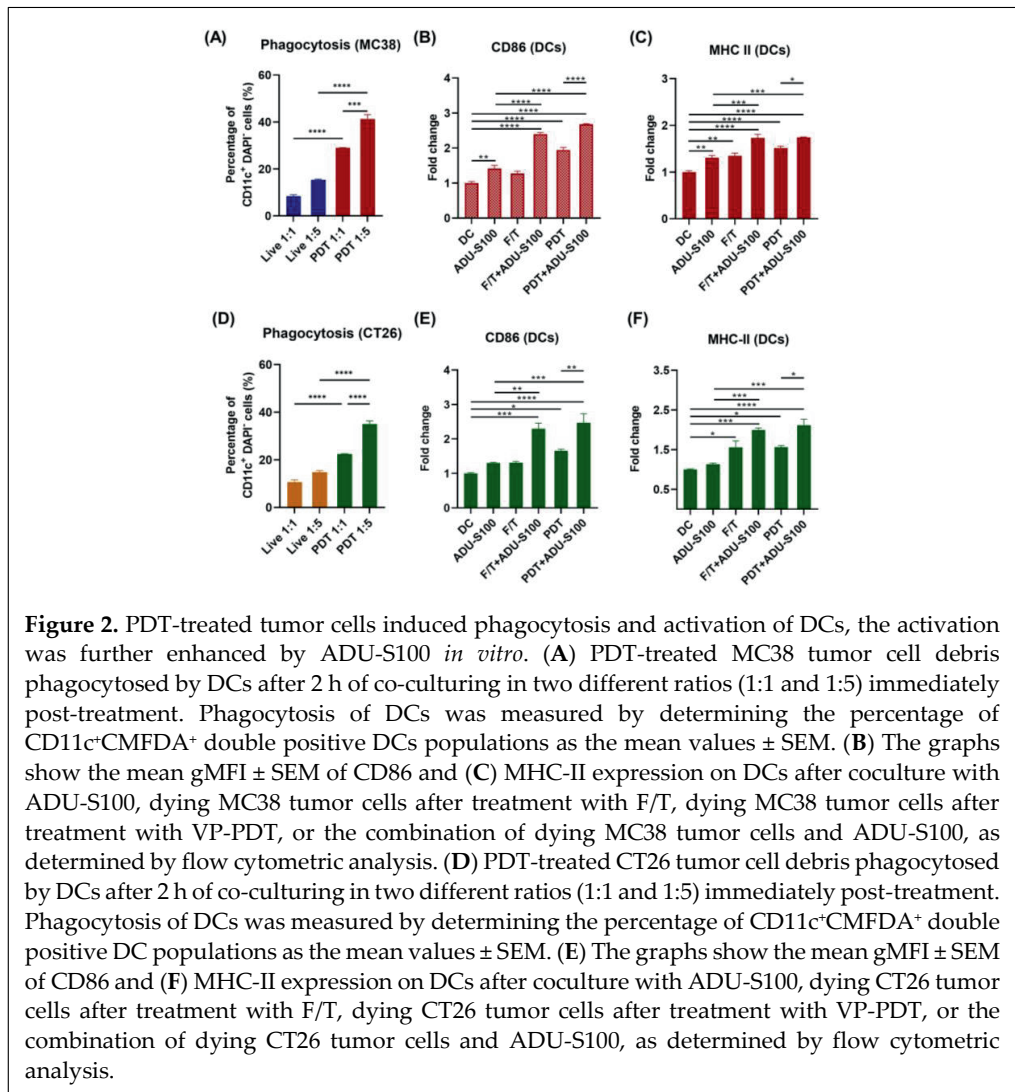
Similar results were observed with CT26 cells (Figure 1E-H; Supplementary Fig.1B; Supplementary Fig.1F-H). In conclusion, the results indicate that VP can be rapidly absorbed by tumor cells and by itself is not directly toxic to tumor cells in the absence of light irradiation. However, it can effectively cause cancer cell death after exposure to light from a 690 nm laser.



3.2. Immunological effects of PDT-treated cancer cells and combination with ADU-S100

Previous studies have clarified that PDT-treated tumor cells can be engulfed by immature DCs *in vitro* [34]. Similarly, we observed that only debris from dying MC38 cells was effectively engulfed by DCs, in contrast to untreated live tumor cells. The percentage of fragment engulfment increased with a higher percentage of tumor cells (Figure 2A). Next, we studied the immunological effects of PDT-treated tumor cells in combination with or without ADU-S100 on DCs and found increased CD86 and MHC-II expression on DCs exposed to dead MC38 cell debris or F/T treatment (Figure 2B, C). In addition, DCs incubated with both tumor cells, which received a combination of PDT and ADU-S100, expressed the highest level of CD86 and MHC-II on their cell surface, which was statistically different for our single treatments (Figure 2B, C; Supplementary Fig.2). Moreover, PDT-induced dying CT26 cells could be phagocytosed by DCs (Figure 2D), which in turn stimulated the phenotypic maturation of DCs. We also found that ADU-S100 amplified this immunological effect of PDT-treated CT26 cells on DC activation, as shown by the increased expression of CD86 and major histocompatibility complex (MHC)-II (Figure 2E, F). However, after DCs were co-cultured with PDT-treated tumor cells and ADU-S100, no significant trend in CD40 expression levels was found compared to the control group.

To examine the effect of PDT-treated cells on macrophage polarization, we co-cultured BMDMs with PDT-induced dying tumor cells. Although PDT-treated cells did not alter the polarization state of bone marrow-derived macrophages (BMDMs) *in vitro*, treatment with ADU-S100 could re-polarize anti-inflammatory M2-type BMDMs [4] toward the proinflammatory M1 phenotype; shown by the increased mRNA expression of M1 markers, surface polarization protein level and production of inflammatory mediators, as well as the decreased expression of key M2 markers (Supplementary Fig. 3). Together, our results suggest that the exposure of DCs to PDT-treated cancer cell debris has an immunological impact on the phagocytosis and maturation *in vitro* and this activation effect of PDT-generated tumor cells on DCs could be enhanced by ADU-S100. In addition, we confirmed the critical role of ADU-S100 for inducing repolarization of BMDMs from M2 to M1.



3.3. PDT in combination with ADU-S100 inhibits tumor growth and increases the survival rate of colon tumor-bearing mice

The accumulation of PS at tumor sites is a prerequisite for PDT. VP has been reported to display absorbance and fluorescence emission in the NIR wavelength region [35] and advantageous fluorescence quantum yield [36]. To validate the accumulation of VP at tumor areas, we acquired optical and PA images after i.v. injection of VP. We confirmed that VP efficiently accumulated in tumors, reached its maximum intensity at 3 h and then gradually decreased with time until 24 h. Notably, strong fluorescence was also detected in the liver and kidneys, which may be due to the clearance of VP by these organs (Supplementary Fig.4B, C). The PA spectra were then first obtained *in vitro*, showing the detectability of VP by PA imaging (Supplementary Fig.4D, E). Further, we acquired PA images over a cross section of the tumor and observed a significantly higher signal in the tumor region than in the surrounding tissue post-injection (Supplementary Fig.4F, G). Altogether, we confirmed that VP efficiently accumulated in tumors but was also found in metabolic organs. Importantly, since the near-infrared (NIR)-laser is a local treatment, no side effect is expected in other organs.

We next investigated the anti-tumor effects of combinational therapy in immunocompetent syngeneic CRC mouse models. Eight days after MC38 tumor cell implantation, different subgroups of mice received mock treatment (PBS), single treatments (PDT or ADU-S100), or the combinational therapy (PDT+ADU-S100). Over the course of our *in vivo* study (Figure 3A), changes in tumor size were recorded. All treatment modalities showed a much slower growth rate at two weeks post-treatment compared to the fast-growing tumors in the control group. The combination of PDT with ADU-S100 exerted a highly suppressive effect on tumor growth and cell proliferation compared to the mild and moderate effects of PDT and ADU-S100, respectively (Figure 3B). Notably, as weight change can act as an important parameter to assess toxicity or damage during treatment, no significant weight loss was observed during the experiment. However, the mice exhibited a slight weight loss within two days in groups, which received ADU-S100 or combinational therapy, but rapidly returned to pre-treatment levels in the subsequent period (Supplementary Fig5A). This might be due to anesthesia and intratumoral injection resulting in a negative effect on the food consumption of these mice. After day 19, all mice gained weight, indicating that the toxicity induced by the treatments was acceptable (Supplementary Fig5A). In addition, the standard survival curve (Kaplan-Meier), which describes the direct effects of treatment on tumor growth, showed that both monotherapies and combinational therapy were able to prolong the survival time of tumor-bearing mice. Notably, combinational therapy eradicated almost all MC38 tumors and approximately half of the tumors resumed growth after ADU-100 treatment. Specifically, the group that received the combinational therapy showed a higher survival rate (91%) compared to the monotherapy groups with PDT (22%) and ADU-S100 (64%; Figure 3C). The related individual tumor MC38 tumor growth during observed period were shown in Figure 3D and the same trend anti-tumor effects of combinational therapy was confirmed in the CT26 model (Supplementary Fig.5B-E).

Tumor ablation ability of single and combinational therapy were also proved by H&E staining and Ki67 staining. We dissected tumor-bearing mice on day 10, when treatment effects on tumor size started to become macroscopically evident and analyzed the changes in tumor pathology by H&E staining. As shown in Figure 3E, a large number of tumor cells with large nuclei and abundant vascular interstitium were visible in the control section. In contrast, in the treatment groups, the membranes of some tumor cells were disrupted and fused with intercellular material to form faint erythema, the damage extent was mildest in PDT group, moderate in ADU-S100 group, and highest in the combinational therapy group. Moreover, monotherapies or combinational therapy both showed inhibitory effects on tumor cell proliferation (Figure 3E). Overall, these data suggest that either PDT or ADU-S100 had an inhibitory effect on the progression of tumor growth, but the combinational therapy was able to effectively control tumor growth and significantly improve survival time of MC38 tumor bearing mice.

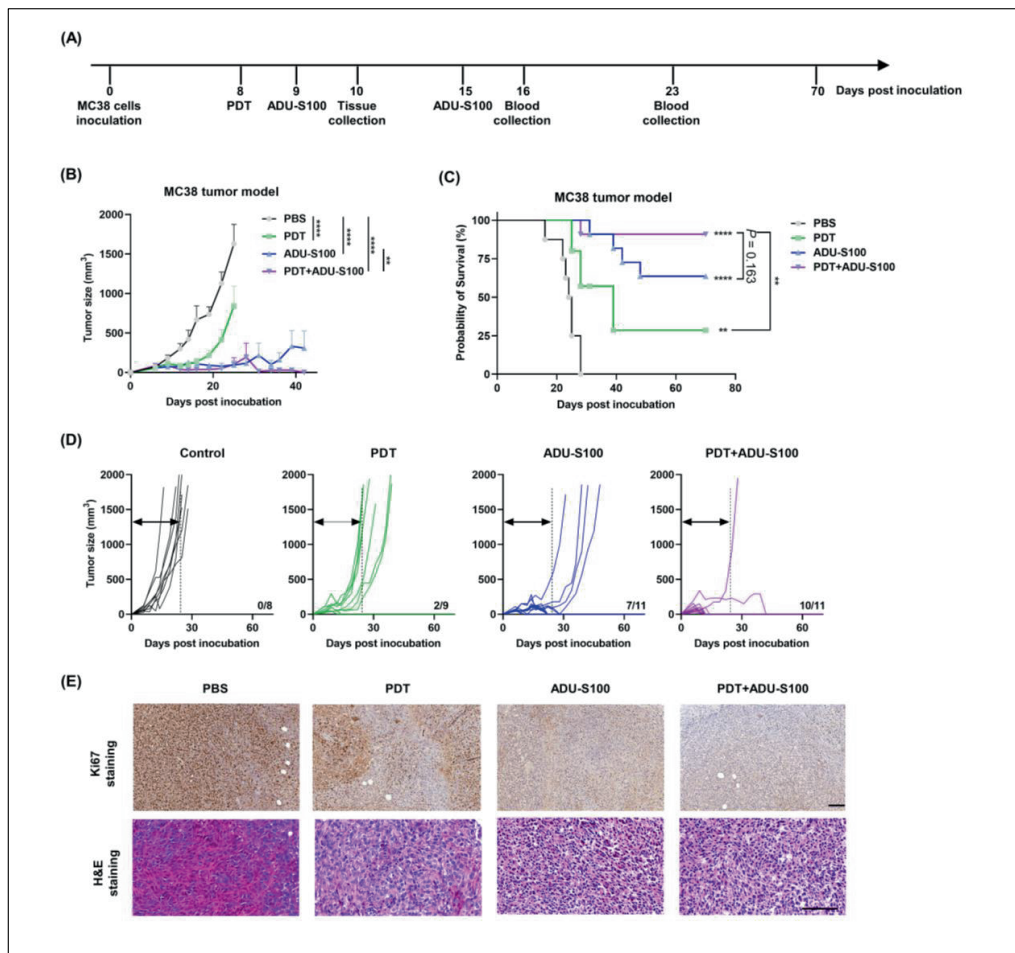


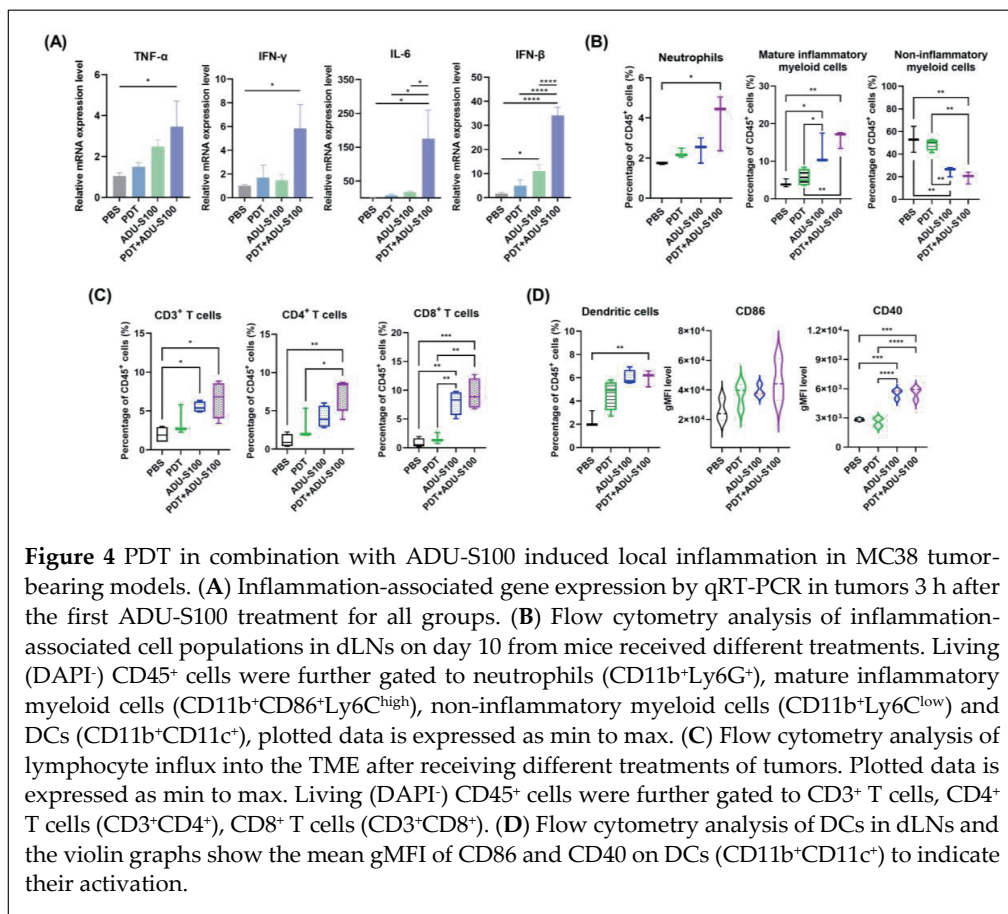
Figure 3 Anti-tumor effects of PDT in combination with ADU-S100 in MC38 tumor-bearing model. **(A)** Schematic representation of the time course and regimen of administration for MC38 tumor-bearing mice. **(B)** Tumor-bearing mice were treated with PDT and, the next day, two intra-tumoral injections of ADU-S100 were administered at one-week intervals. Average tumor size of MC38 tumors over time, and data is expressed as mean \pm SEM: Control vs. PDT $p < 0.0001$; Control vs. ADU-S100 $p < 0.0001$; Control vs. PDT + ADU-S100 $p < 0.0001$; PDT vs. PDT + ADU-S100 $p < 0.0001$; ADU-S100 vs. PDT + ADU-S100 $p = 0.0015$. The log-rank test was used to assess the statistical significance of survival time. Two-way ANOVAs were used for the statistical analysis of significance of tumor volume and statistical differences were considered significant at $*p < 0.05$, $**p < 0.01$, $***p < 0.001$, $****p < 0.0001$. **(C)** Percentage survival of MC38 tumor-bearing mice receiving different treatments: Control vs. PDT $p = 0.0019$; Control vs. ADU-S100 $p < 0.0001$; Control vs. PDT + ADU-S100 $p < 0.0001$; PDT vs. PDT + ADU-S100 $p = 0.0065$; ADU-S100 vs. PDT + ADU-S100 $p = 0.1627$. The log-rank test was used to assess the statistical significance of survival time and statistical differences were considered significant at $*p < 0.05$, $**p < 0.01$, $***p < 0.001$, $****p < 0.0001$. **(D)** Individual MC38 tumor growth in different treatment groups; the numbers above the right corner of the x-axis in each graph represent the percentage of mice that achieved complete tumor regression. **(E)** Representative H&E and Ki67 staining images of tumors on day 10 after the mice received different treatments. Scale bar = 100 μ m.

3.4. PDT in combination with ADU-S100 induces an acute inflammatory state and immune activation in colon tumor-bearing mice

PDT and ADU-S100 have been reported to exert anti-tumor effects by converting the TME and the tumor-draining lymph nodes (dLNs) from an immunosuppressive to a proinflammatory state [11,37]. As shown in Figure 4A, three hours after the first ADU-S100 treatment, tumors treated with combinational therapy showed locally higher expression of genes encoding proinflammatory cytokines: TNF- α , IFN- γ , IL-6, and IFN- β in compared to tumors subjected to single treatments. These cytokines play a key role during initial inflammation and the transition to T-cell-mediated immune responses. Thereafter, we analyzed the immune cell populations in the tumor, spleen and dLNs on day 10. The tumors treated with the combination exhibited significantly more infiltration of cytotoxic T lymphocytes (CTLs, CD8⁺ T cells) than helper T cells (CD4⁺ T cells) into the TME compared to tumors treated with monotherapies or control (Figure 4B). Of note, changes in the proportions of CD4⁺ lymphocytes and CTLs in the spleen and dLNs were not significantly different, but treatment alone and combinational therapy was found to increase the proportion of IFN- γ or TNF- α positive CD8⁺ T cells in the spleen and lymph nodes, although only to a small extent (Supplementary Fig.6).

Importantly, dLNs can have a profound impact on the antigen presentation as well as on immune responses due to their anatomical setting downstream from the tumors [38]. Rapid recruitment of and an increase in neutrophil numbers are manifestations of acute inflammation and can initiate anti-tumor adaptive immune responses under inflammatory conditions [39]. The results showed that either treatment alone or combinational therapy induced the formation of proinflammatory dLN state, but combinational therapy triggered the most significant changes, including infiltration of dLNs by neutrophils, increasing levels of mature inflammatory myeloid-derived cells and decreasing proportions of noninflammatory myeloid-derived cells (Figure 4C). Moreover,

we observed that all treatment groups induced the infiltration of DCs into the dLNs, but only significantly changed in dLNs from combinational therapy -treated mice (Figure 4D). All treatments promoted the activation of DCs in dLNs, as evidenced by an increase in CD86 and CD40 expression on DCs. In addition, combinational therapy further increased the expression of CD86, but not CD40, in a non-significant amount, when compared to treatment alone (Figure 4D). These data correspond to our *in vitro* co-culture model results. In conclusion, our findings proved that combinational therapy amplifies the effect of monotherapies on immune-enhancing transformation of the TME Figure 4 and dLNs.



3.5. PDT in combination with ADU-S100 induces systematic anti-tumor immunity

Local treatments have the potential to trigger systemic immune responses and, in some cases, the potential to exert an abscopal effect [40]. Hence, we examined the levels of circulating lymphocytes and total serum immunoglobulin G (IgG) in mice that received different treatments. On day 16, few changes and moderate increases in circulating CD3⁺ and CD4⁺ lymphocytes and CTLs were observed in PDT-treated mice and ADU-S100-treated mice. Importantly, the combination treatment significantly increased the levels of CD3⁺ and CD4⁺ T cells in the blood compared to PDT, and the increase in CTLs in the

combined treatment group was significantly higher compared to the monotherapy groups (Figure 5A, B). In contrast, there was no difference in blood-circulating lymphocytes of mice receiving single or combinational therapy on day 23 (Supplementary Fig.7A).

Previous studies have shown that CD4⁺ helper T cells can interact with B cells, leading to the ability of B cells to activate antibodies through a T cell-dependent pathway [41]. Given the important role of CD4⁺ T cells on day 23, we investigated blood B cell activation to explore this possibility. Although no changes in the total number of CD19⁺ B cells were observed between groups (Supplementary Fig.7B), the gMFI for CD40 expression, a co-stimulatory marker on CD19⁺ B cells, was increased after all treatments with the significant enhancement only in combinational therapy, when compared with the PBS-treated group. In contrast, the CD86 expression of CD19⁺ B cells did not show any changes (Supplementary Fig.7C). Subsequently, we measured the IgG concentration in total serum. As shown in Figure 5C, PDT induced a slight increase in IgG secretion, whereas ADU-S100 stimulation induced a modest increase. Strikingly, the intensity of IgG in the serum of combinational therapy-treated mice was significantly improved compared to that of mice receiving PDT alone, but not to the ADU-S100-treated group. These data collectively suggest that the combinational therapy could establish systemic immune responses *in vivo*, including enhanced proliferation of lymphocytes and antibody production in peripheral blood, which is essential for complete tumor eradication.

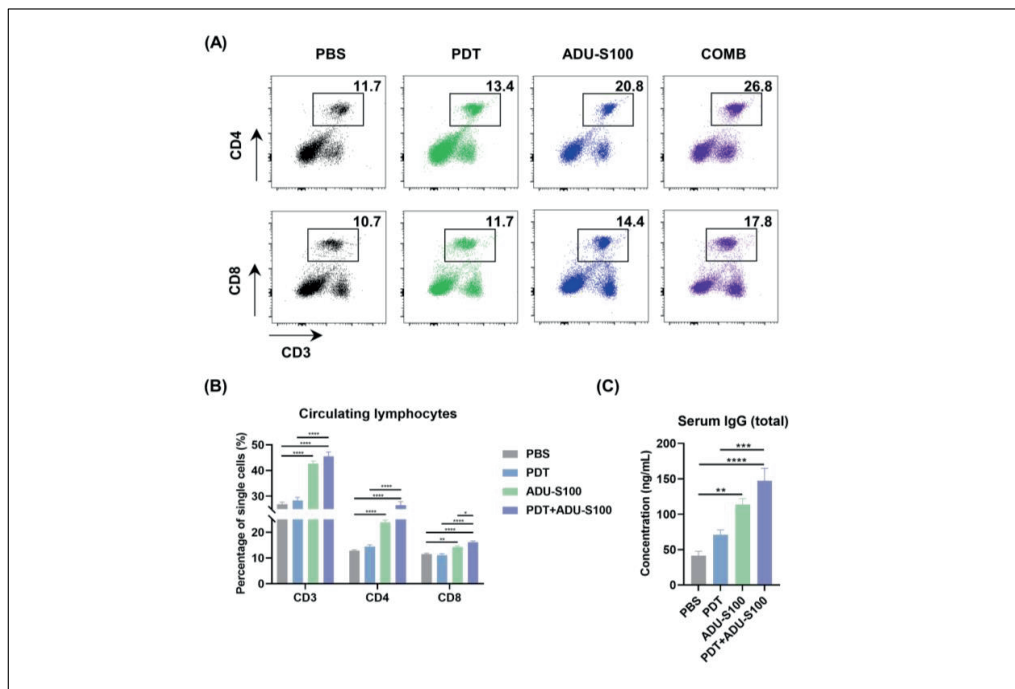
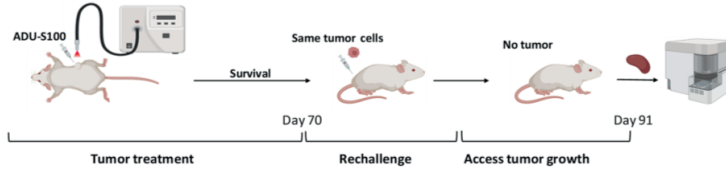


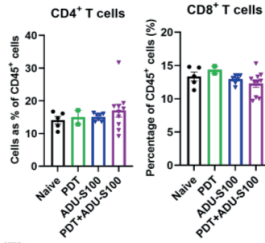
Figure 5 The combination of PDT and intratumoral injection of ADU-S100 boosted systematic anti-tumor immunity. (A) Representative flow cytometry plot showing the proportions of circulating CD4⁺ and CD8⁺ T cells from MC38 tumor-bearing mice in different subgroups on day 16. (B) Statistical evaluation of percentage of circulating CD3⁺, CD4⁺ and CD8⁺ T cells. Data is expressed as mean ± SEM (**p* < 0.05, ***p* < 0.01, ****p* < 0.001, *****p* < 0.0001). (C) Total serum IgG concentrations of MC38 tumor-bearing mice in different subgroups on day 23 were assessed by ELISA. Data is expressed as mean ± SEM.

3.6. Effective immune memory efficacy upon PDT combined with ADU-S100 treatment persists in tumor-free mice

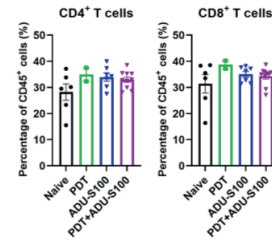
We next examined the potential of established peripherally initiated systemic immunity to produce long-term immune memory and regulate distant tumors (Figure 6A). Indeed, the mice that were cured by monotherapy and combinational therapy all resisted tumor growth after rechallenging; this was in contrast to naïve controls that exhibited rapid tumor growth, suggesting the development of a functional immune memory against the same type of cancer. To better understand the establishment of the immune memory function, we studied the phenotype of immune memory T cells in the blood, dLNs, and spleen of these cured mice. As shown in Figure 6B, C, we found no significant differences in the number of CD4⁺ and CD8⁺ T cells in blood and dLNs in all cured mice from treatment groups. However, CD4⁺ T cells in the spleen were significantly higher in the cured mice after initial ADU-S100 alone and combinational therapy group (Figure 6D). All cured mice exhibited a slight increase in functional memory CD4⁺ and memory CD8⁺ T cells in the blood compared to the naïve control mice, while only the combinational therapy -treated survivors exhibited a significant increase of CD8⁺ central memory T cells in the blood when compared to control (Figure 6E). In the dLNs, healed tumor-free mice in the ADU-S100 group and combinational therapy group showed higher levels of central memory and effector memory CD4⁺/CD8⁺ T cells and the mice that were cured by combinational therapy exhibited the most significant changes (Figure 6F). Similarly, significantly more memory CD4⁺ T cells were found in the spleen of combinational therapy-treated mice during this rechallenge (Figure 6G). This finding suggests that combinational therapy resulted in the most prominent development of systemic memory immunity after initial tumor cell challenge and subsequent rechallenge after tumor eradication.

(A)**(B)**

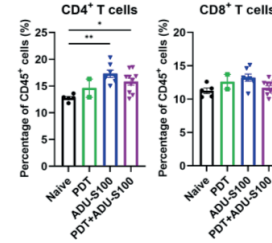
Blood (after rechallenge)

**(C)**

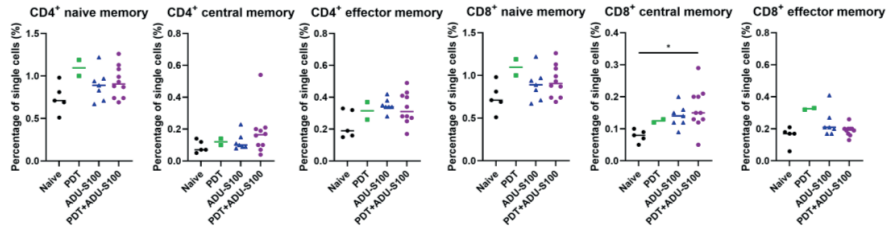
dLNs (after rechallenge)

**(D)**

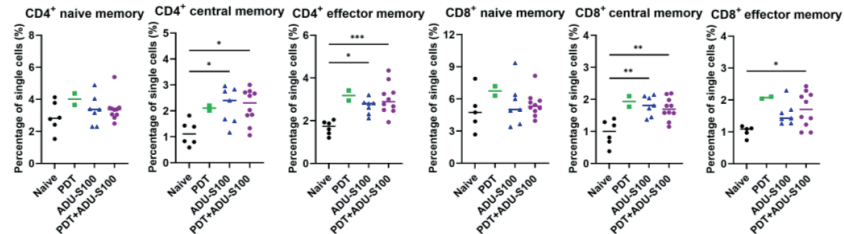
Spleen (after rechallenge)

**(E)**

Blood (after rechallenge)

**(F)**

dLNs (after rechallenge)

**(G)**

Spleen (after rechallenge)

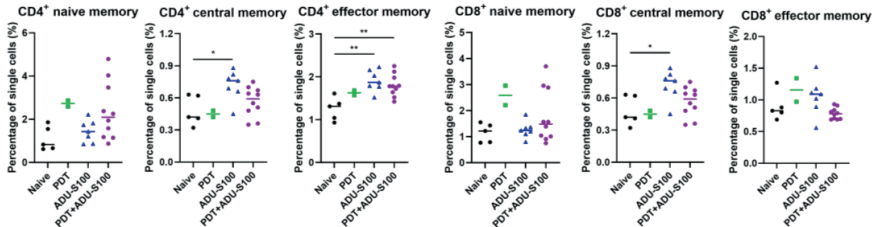


Figure 6 Cured mice after treatment with PDT in combination with ADU-S100 obtained a long-term immune memory. (A) Schematic representation of the time course and regimen of administration for MC38 tumor-bearing mice. (B) Percentages of CD4⁺ T lymphocytes and CD8⁺ T lymphocytes in the blood, (C) dLNs, and (D) spleen of mice that received different treatments 21 days after rechallenging. (E) Proportions of immune memory T cells, including CD4⁺ central memory T cells (CD3⁺CD4⁺CD44⁺CD62L⁺), CD4⁺ effector memory T cells (CD3⁺CD4⁺CD44⁺CD62L⁻), CD4⁺ naïve memory T cells (CD3⁺CD4⁺CD44⁻CD62L⁺), CD8⁺ central memory T cells (CD3⁺CD8⁺CD44⁺CD62L⁺), CD8⁺ effector memory T cells (CD3⁺CD8⁺CD44⁺CD62L⁻), and CD8⁺ naïve memory T cells (CD3⁺CD8⁺CD44⁻CD62L⁺) in the blood, (F) dLNs and (G) spleen of mice that received different treatments 21 days after rechallenge.

3.7. PDT in combination with ADU-S100 inhibits distant tumor growth in mice bearing bilateral MC38 tumors

Moreover, we used the dual-MC38-derived tumor-bearing mice model, i.e., one tumor on each flank, to mimic the clinical situation of primary tumors and smaller metastases. We treated only one tumor using the same protocol as described above (Figure 3A). Consistent with previous results in the single tumor model (Figure 3B, C), in comparison to fatal tumor growth progression in the control group, tumors receiving direct treatments had a slow growth curve and combinational therapy was the most effective against tumor progression (Supplementary Fig.8A). At three weeks post-inoculation, both monotherapies and combinational therapy resulted in delayed untreated tumor growth and inhibited total tumor burden compared to the PBS group, with both ADU-S100 treatment and combinational therapy exhibiting the strongest effects (Supplementary Fig.8A). Individual MC38 tumor growth of treated and untreated tumors (mm³) in different treatment groups are shown in Supplementary Fig.8B. Although the combination treatment did not exert a higher tumor control effect on the distant untreated tumors than ADU-S100 treatment alone, it increased the survival rate of the mice bearing two MC38 tumors. Two of the five mice of treated tumors were completely controlled, and distant tumors were eradicated. In contrast, none of the mice in the PDT-treated group and only one out of five mice in the ADU-S100-treated group showed long-term survival (Supplementary Fig.8C). A similar effect of delaying untreated tumor growth was also observed in the CT26 bilateral model (Supplementary Fig.9). In conclusion, our results suggest that combinational therapy provides a systemic anti-tumor immune response in mice bearing colon tumors, including primary and distant tumors.

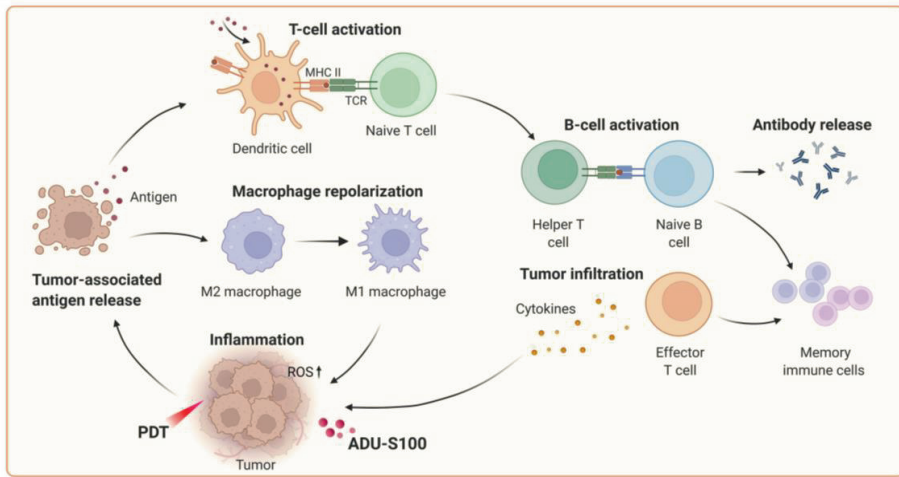


Figure 7 Schematic illustration of our current working model by which PDT in combination with a STING agonist (ADU-S100) elicits antitumor immunity in colorectal cancer. The diagram was created with biorender.com.

4. Discussion

The therapeutic effect of PDT is usually not sufficient to induce a complete and lasting tumor-inhibiting effect in immunosuppressive “cold” tumors [11,12]. Here, we present our preclinical study to evaluate PDT in combination with ADU-S100, a powerful, safe and effective STING agonist and thereby offering a clinically translatable improvement for the utilization of PDT in solid tumors. For the first time, we demonstrated that PDT combined with ADU-S100 enhances anti-tumor effects *in vivo*, induces local inflammation, and enhances anti-tumor immune responses as well as induces long-term immunological memory in murine CRC models (MC38, CT26). Furthermore, we found that the metastatic capacity of tumors was significantly inhibited by combinational therapy due to the effect on the distant tumor in a double-tumor model. This revealed the promising future of combinational therapy for inhibiting tumor recurrence, migration, and metastasis.

Our *in vitro* results show that VP can be rapidly taken up into the cytoplasm of murine CRC cell lines and induce effective cell death after irradiation [42]. DCs maturation is a preliminary step to initiate anti-tumor immune response [43]. Data here shows that PDT-induced dying tumor cells can be phagocytosed by DCs and thus induce activation of DCs, as shown by increased expression of CD86 and MHC-II, which is consistent with the concept that PDT-treated cells are immunogenic [44-46]. This may be due to the fact that apoptosis and necrosis-induced cell death can provoke a response from the immune system [47,48]. However, we did not detect strong evidence for the ability of VP-PDT to act as an immunogenic cell death inducer. Especially, we did not observe changes in the expression of damage-associated molecular patterns (DAMPs) that are an indication of immunogenic cell death due to the ability to interact with APC or other immune cells, including heat shock proteins (HSP)-70, calreticulin (CRT), and adenosine triphosphate (ATP) release. Furthermore, ADU-S100 amplified this immunological effect of PDT-

treated cells on DC activation. Macrophages are another important type of immune cell [49]. *In vitro*, we did not observe effects of PDT-treated cells but ADU-S100 on the re-education of M2-type BMDMs, which promote tumor growth, towards the M1 phenotype which are tumor growth repressive. Repolarization of the TME may also be one of the mechanisms of action of ADU-S100 due to the initiation and activations of IFN type I pathways in the TME. Therefore, our future studies will also explore the unique role of macrophages in combinational therapy.

In contrast to human xenograft tumors, the current study used the immunocompetent syngeneic tumor mice model to investigate the effect of combinational therapy on immune functions, which is more suitable for the translation of subsequent treatment strategies for clinical application in the field of cancer [50]. We investigated not only the anti-tumor capacity of combinational therapy but also the immunological mechanisms of anti-tumor immunity. First, tumor-bearing mice were treated with PDT and, the next day, two intratumoral injections of ADU-S100 were administered at one-week intervals. We found the combinational therapy almost completely eradicated MC38 tumors, prolonged the survival of tumor-bearing mice, and showed the same trend in the CT26 model. The underlying mechanism, according to our data, is that combinational therapy initiates local inflammation in the tumor which subsequently establishes systemic immune responses, including cellular and humoral immunity as observed in blood, spleen and dLNs.

Based on the knowledge that PDT treatment disrupts blood vessels within 24 h after treatment, induces an inflammatory response, and subsequently leads to the accumulation of DCs and lymphocytes at the tumor site for 1-7 days [51], we investigated the anti-tumor immunity of tumor-bearing mice on day 10 (48 h after PDT). We found stronger tumor ablation with the combinational therapy than with the monotherapies, accompanied by a stronger inflammatory state within the tumor due to increased expression of pro-inflammatory cytokines mRNA, which is a driving factor during the initial inflammation and the transition to T cell-mediated immune responses [52]. This finding is in accordance with previous findings that STING agonist can promote inflammatory pathways following the release of tumor antigens by radiation therapy to synergistically treat pancreatic tumors in mice [38]. Increased infiltration of CD4⁺ helper cells and CD8⁺ cytotoxic T effector cells were found in the TME. On one hand, the reason behind this may be the superimposed vascular disruption capacity of PDT and ADU-S100, with endothelial cell damage further leading to more severe local inflammation [26-28,53]. On the other hand, the local ablation of tumors by PDT provides additional tumor-associated antigens to ADU-S100-activated DCs and activates adaptive immune responses [54-56]. Moreover, our results showed that treatment alone or combinational therapy increased the dLNs infiltration by neutrophils, increased levels of inflammatory myeloid-derived cells, and decreased levels of non-inflammatory myeloid-derived cells, with the ADU-S100 and combinational therapy groups showing the most significant changes. These results are coincided with the important role of myeloid immune cells during PDT or ADU-S100 treatment [57,58]. Furthermore, our *in vivo* results demonstrate that combinational therapy enhanced DCs activation in dLNs by means of a moderate increase of CD86 expression and a slightly increase of CD40 expression, which is similar

to our *in vitro* co-culture data. This also validates our previous assumption that PDT-treated cells provide antigens for ADU-S100-activated DCs. Our findings suggest that combinational therapy can promote tumor ablation by altering the “cold” TME and dLNs to an immune responsive state.

Next, we examined the changes in circulating lymphocytes in the blood of mice receiving different treatments at two different time points. On day 16, little change was observed in CD3⁺, CD4⁺, and CD8⁺ T cells in PDT-treated mice. However, ADU-S100-treated mice showed a moderate increase, while the combinational therapy demonstrated the highest levels of lymphocytes in the blood of tumor-bearing mice. This reveals that PDT alone is only able to elicit a limited immune response and underlines the additive advantages of combinational therapy [12,13,59]. On day 23, no significant immune response was observed for CD4⁺, but a decrease for CD8⁺ T cells and an elevated expression of co-stimulatory CD40 on CD19⁺ B cells as well as increased IgG levels in blood serum were observed in all groups. This was probably mediated by the activation of CD4⁺ and CD8⁺ cells that subsequently produce IFN- γ which in turns can activate CD19⁺ B-cells for isotype switching to produce more IgG [60-62]. These results contrast with our findings on day 16, when we did not detect antibodies but changes in circulating T cells, which could be explained by the fact that at a later time point (day 23) humoral immune response took over the role of the adaptive immune response against residual tumor cells and generated immune memory capacity [14]. Our data provides a theoretical basis for achieving relapse prevention and further enhancing the ectopic effect through systemic treatment triggered by combinational therapy.

To test our hypothesis of protection from tumor recurrence by combinational therapy, previously cured mice were rechallenged by another injection of homologous tumor cells. All of the previously cured mice rejected the tumor rechallenge, while the naive controls showed rapid tumor growth. Further analysis of the phenotype of memory T cells showed that their differentiation followed a linear path: naive \rightarrow effector \rightarrow central [63]. Our results suggest that either monotherapy (PDT or ADU-S100) or combinational therapy is capable of producing long-lasting immune memory capacity, although only combinational therapy-treated mice produced statistically significant changes in memory T cells, when compared to controls. In particular, in comparison to control group, most significant changes occurred in the dLNs of initial combinational therapy healed mice and lagging effector memory T cells and central memory T cells in dLNs may be the fastest line of defense when tumor cells attack the organism again [64].

Finally, we examined the abscopal effect of PDT combined with ADU-S100 in CRC models bearing bilateral tumors. Primary tumor growth was inhibited or ablated by PDT or ADU-S100 or the combinational therapy. Although the combinational therapy did not demonstrate a higher tumor control effect on the distant, untreated tumor than the ADU-S100 treatment alone, it prolonged the survival of the double tumor-bearing mice. Being consistent with our results, PDT and intratumoral STING agonist treatment alone were able to control untreated distant tumor, as has been shown by Liu Zhuang *et al.* and Ignacio Melero *et al.*, respectively [65,66]. The efficiency of combinational therapy was also assessed in the CT26 colon cancer tumor model. All treatments were performed as

described above in either the unilateral tumor model or the bilateral tumor model and a similar trend but relatively limited tumor suppression as in the MC38 model was observed.

In conclusion, we provided first-hand evidence of the regulation of tumor progression and the induction of immunological memory by combinational therapy in CRC mouse models. The rationale underlying our current working model could be as follows in Figure 7: 1). NIR irradiation allowed the photosensitizer to directly kill tumor cells via ROS but induced insufficient immune responses. 2). The combination of PDT and intratumoral ADU-S100 induced an inflammatory state in the TME and dLNs, thereby leading to a series of immune responses, including adaptive cellular and humoral immune responses. 3). ADU-S100 promotes the repolarization of M2 macrophages toward the M1 phenotype, relieving their immune inhibitory effects. Further studies are needed to identify the function of important factors in the TME, such as other immune cells and endothelial cells, during treatment.

References

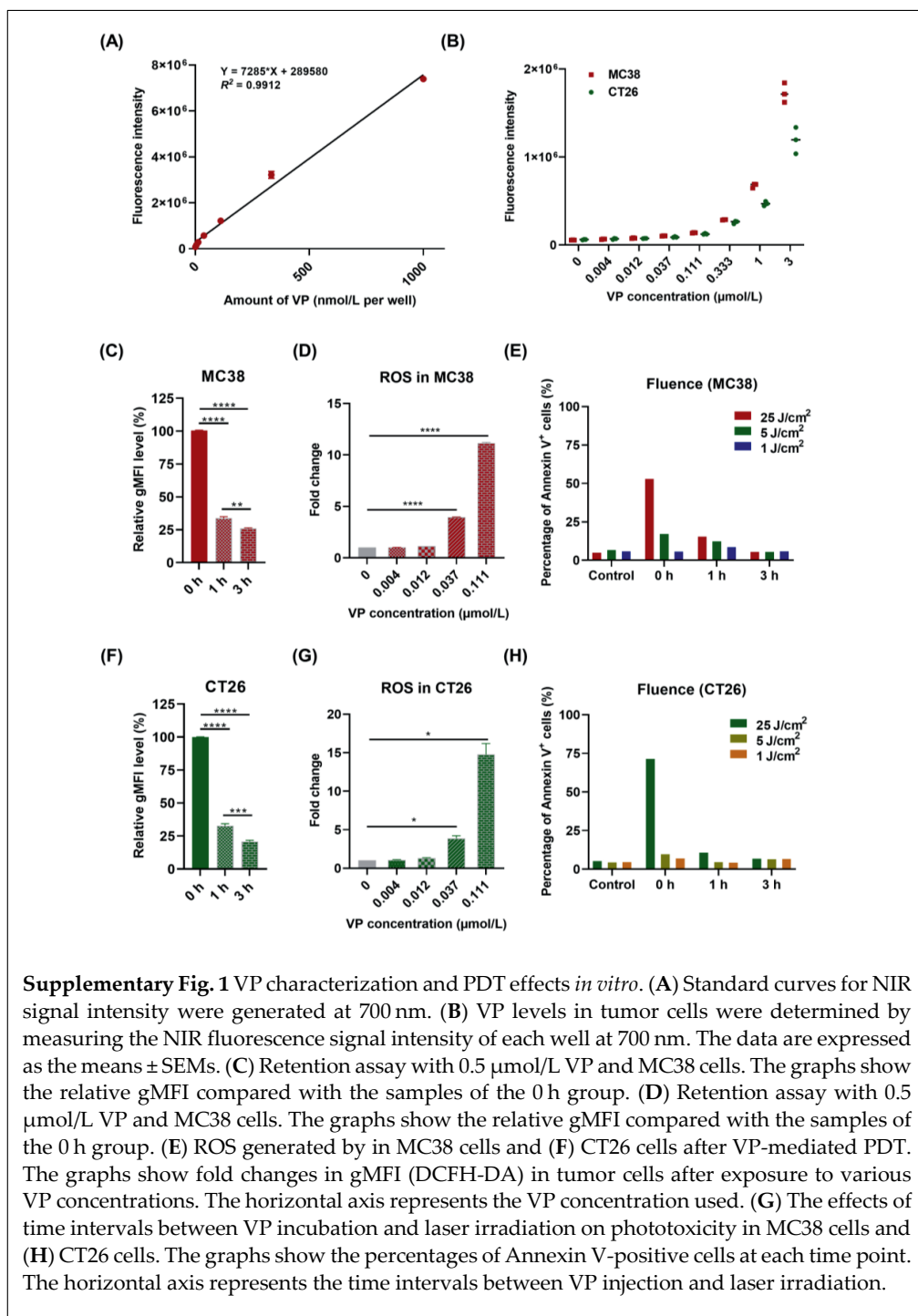
1. Siegel RL, Miller KD, Fuchs HE, Jemal A. Cancer statistics, 2022. *CA Cancer J Clin.* 2022;72(1):7-33. [http:// doi:10.3322/caac.21708](http://doi:10.3322/caac.21708)
2. Xi Y, Xu P. Global colorectal cancer burden in 2020 and projections to 2040. *Transl Oncol.* 2021;14(10):101174. [http:// doi:10.1016/j.tranon.2021.101174](http://doi:10.1016/j.tranon.2021.101174)
3. Ahmed M. Colon Cancer: A Clinician's Perspective in 2019. *Gastroenterology Res.* 2020;13(1):1-10. [http:// doi:10.14740/gr1239](http://doi:10.14740/gr1239)
4. C de S L Oliveira AL, Schomann T, de Geus-Oei LF, Kapiteijn E, Cruz LJ, de Araújo Junior RF. Nanocarriers as a Tool for the Treatment of Colorectal Cancer. *Pharmaceutics.* 2021;13(8):1321. [http:// doi:10.3390/pharmaceutics13081321](http://doi:10.3390/pharmaceutics13081321)
5. Dolmans DE, Fukumura D, Jain RK. Photodynamic therapy for cancer. *Nat Rev Cancer.* 2003;3(5):380-387. [http:// doi:10.1038/nrc1071](http://doi:10.1038/nrc1071)
6. Guidolin K, Ding L, Yan H, et al. Photodynamic Therapy for Colorectal Cancer: A Systematic Review of Clinical Research. *Surg Innov.* 2022;15533506221083545. [http:// doi:10.1177/15533506221083545](http://doi:10.1177/15533506221083545)
7. Dougherty TJ, Gomer CJ, Henderson BW, et al. Photodynamic therapy. *J Natl Cancer Inst.* 1998;90(12):889-905. [http:// doi:10.1093/jnci/90.12.889](http://doi:10.1093/jnci/90.12.889)
8. Allison RR, Moghissi K. Photodynamic Therapy (PDT): PDT Mechanisms. *Clin Endosc.* 2013;46(1):24-29. [http:// doi:10.5946/ce.2013.46.1.24](http://doi:10.5946/ce.2013.46.1.24)
9. Chen B., Pogue B., Hoopes P., Hasan T. Vascular and cellular targeting for photodynamic therapy. *Crit. Rev. Eukaryot. Gene Expr.* 2006;16(4):279-305. [http:// doi:10.1615/CritRevEukarGeneExpr.v16.i4.10](http://doi:10.1615/CritRevEukarGeneExpr.v16.i4.10)
10. Michels S, Schmidt-Erfurth U. Sequence of early vascular events after photodynamic therapy. *Invest Ophthalmol Vis Sci.* 2003;44(5):2147-2154. [http:// doi:10.1167/iovs.02-0604](http://doi:10.1167/iovs.02-0604)
11. Castano AP, Mroz P, Hamblin MR. Photodynamic therapy and anti-tumour immunity. *Nat Rev Cancer.* 2006;6(7):535-545. [http:// doi:10.1038/nrc1894](http://doi:10.1038/nrc1894)
12. Falk-Mahapatra R, Gollnick SO. Photodynamic Therapy and Immunity: An Update. *Photochem Photobiol.* 2020;96(3):550-559. [http:// doi:10.1111/php.13253](http://doi:10.1111/php.13253)
13. Kawczyk-Krupka A, Bugaj AM, Latos W, et al. Photodynamic therapy in colorectal cancer treatment-The state of the art in preclinical research. *Photodiagnosis Photodyn Ther.* 2016;13:158-174. [http:// doi:10.1016/j.pdpdt.2015.07.175](http://doi:10.1016/j.pdpdt.2015.07.175)
14. Park J, Lee YK, Park IK, Hwang SR. Current Limitations and Recent Progress in Nanomedicine for Clinically Available Photodynamic Therapy. *Biomedicines.* 2021;9(1):85. [http:// doi:10.3390/biomedicines9010085](http://doi:10.3390/biomedicines9010085)
15. Kim, W.S., Khot, M.I., Woo, H.M. et al. AI-enabled, implantable, multichannel wireless telemetry for photodynamic therapy. *Nat Commun* 2022,13, 2178. [http:// doi:10.1038/s41467-022-29878-1](http://doi:10.1038/s41467-022-29878-1)
16. Gunaydin G, Gedik ME, Ayan S. Photodynamic Therapy-Current Limitations and Novel Approaches. *Front Chem.* 2021;9:691697. <http://10.3389/fchem.2021.691697>
17. Farkona, S., Diamandis, E.P. & Blasutig, I.M. Cancer immunotherapy: the beginning of the end of cancer?. *BMC Med* 2016;14, 73. [https:// doi:10.1186/s12916-016-0623-5](https://doi:10.1186/s12916-016-0623-5)
18. Esfahani K, Roudaia L, Buhlaiga N, Del Rincon SV, Papneja N, Miller WH Jr. A review of cancer immunotherapy: from the past, to the present, to the future. *Curr Oncol.* 2020;27(Suppl 2):S87-S97. [http:// doi:10.3747/co.27.5223](http://doi:10.3747/co.27.5223)
19. Shen, L., Zhou, T., Fan, Y., Chang, X., Wang, Y., Sun, J., Xing L & Jiang, H. Recent progress in tumor photodynamic immunotherapy. *Chinese Chemical Letters*, 31(7), 1709-1716. (2020). [http:// doi:10.1016/j.ccllet.2020.02.007](http://doi:10.1016/j.ccllet.2020.02.007)

20. Garland KM, Sheehy TL, Wilson JT. Chemical and Biomolecular Strategies for STING Pathway Activation in Cancer Immunotherapy. *Chem Rev.* 2022;122(6):5977-6039. <http://doi:10.1021/acs.chemrev.1c00750>
21. Prantner, D.; Perkins, D. J.; Lai, W.; Williams, M. S.; Sharma, S.; Fitzgerald, K. A.; Vogel, S. N. 5,6-Dimethylxanthenone-4-acetic acid (DMXAA) activates stimulator of interferon gene (STING)-dependent innate immune pathways and is regulated by mitochondrial membrane potential. *J. Biol. Chem.* 2012, 287, 39776- 39788, <http://doi:10.1074/jbc.M112.382986>
22. Jiang M, Chen P, Wang L, et al. cGAS-STING, an important pathway in cancer immunotherapy. *J Hematol Oncol.* 2020;13(1):81. <http://doi:10.1186/s13045-020-00916-z>
23. Zheng J, Mo J, Zhu T, et al. Comprehensive elaboration of the cGAS-STING signaling axis in cancer development and immunotherapy. *Mol Cancer.* 2020;19(1):133. <http://doi:10.1186/s12943-020-01250-1>
24. Corrales L, Glickman LH, McWhirter SM, et al. Direct activation of sting in the tumor microenvironment leads to potent and systemic tumor regression and immunity. *Cell Rep* 2015;11:1018-30. <http://doi:10.1016/j.celrep.2015.04.031>
25. Cheng N, Watkins-Schulz R, Junkins RD, et al. A nanoparticle-incorporated STING activator enhances antitumor immunity in PD-L1-insensitive models of triple-negative breast cancer. *JCI Insight.* 2018;3(22):e120638. <http://doi:10.1172/jci.insight.120638>
26. Downey CM, Aghaei M, Schwendener RA, Jirik FR. DMXAA causes tumor site-specific vascular disruption in murine non-small cell lung cancer, and like the endogenous non-canonical cyclic dinucleotide STING agonist, 2'3'-cGAMP, induces M2 macrophage repolarization. *PLoS One.* 2014;9(6):e99988. <http://doi:10.1371/journal.pone.0099988>
27. Chelvanambi M, Fecek RJ, Taylor JL, Storkus WJ. STING agonist-based treatment promotes vascular normalization and tertiary lymphoid structure formation in the therapeutic melanoma microenvironment. *J Immunother Cancer.* 2021;9(2):e001906. <http://doi:10.1136/jitc-2020-001906>
28. Yang H, Lee WS, Kong SJ, et al. STING activation reprograms tumor vasculatures and synergizes with VEGFR2 blockade. *J Clin Invest.* 2019;129(10):4350-4364. <http://doi:10.1172/JCI125413>
29. Chelvanambi M, Fecek RJ, Taylor JL, Storkus WJ. STING agonist-based treatment promotes vascular normalization and tertiary lymphoid structure formation in the therapeutic melanoma microenvironment. *J Immunother Cancer.* 2021;9(2):e001906. <http://doi:10.1136/jitc-2020-001906>
30. Kleinovink JW, Ossendorp F. Combination of Photodynamic Therapy and Immune Checkpoint Blockade. *Methods Mol Biol.* 2022;2451:589-596. http://doi:10.1007/978-1-0716-2099-1_30
31. Schuurhuis DH, Laban S, Toes RE, et al. Immature dendritic cells acquire CD8(+) cytotoxic T lymphocyte priming capacity upon activation by T helper cell-independent or -dependent stimuli. *J Exp Med.* 2000;192(1):145-150. <http://doi:10.1084/jem.192.1.145>
32. Toda G, Yamauchi T, Kadowaki T, Ueki K. Preparation and culture of bone marrow-derived macrophages from mice for functional analysis. *STAR Protoc.* 2020;2(1):100246. <http://doi:10.1016/j.xpro.2020.100246>
33. Kleinovink JW, Ossendorp F. Measuring the Antitumor T-Cell Response in the Context of Photodynamic Therapy. *Methods Mol Biol.* 2022;2451:579-588. http://doi:10.1007/978-1-0716-2099-1_29
34. Doix B,, Tremplec N, Riant O, Feron O. Low Photosensitizer Dose and Early Radiotherapy Enhance Antitumor Immune Response of Photodynamic Therapy-Based Dendritic Cell Vaccination. *Front Oncol.* 2019;9:811. <http://doi:10.3389/fonc.2019.00811>

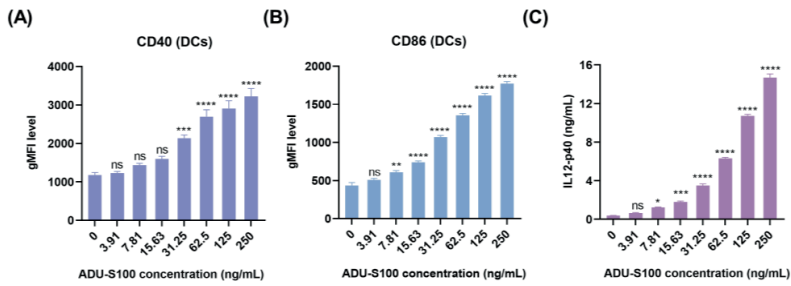
35. Shao P, Chapman DW, Moore RB, Zemp RJ. Monitoring photodynamic therapy with photoacoustic microscopy. *J Biomed Opt.* 2015;20(10):106012. <http://doi:10.1117/1.JBO.20.10.106012>
36. Yu J, Schuman JS, Lee JK, Lee SG, Chang JH, Kim K. A Light Illumination Enhancement Device for Photoacoustic Imaging: In Vivo Animal Study. *IEEE Trans Ultrason Ferroelectr Freq Control.* 2017;64(8):1205-1211. <http://doi:10.1109/TUFFC.2017.2713599>
37. Deng, L.; Liang, H.; Xu, M.; Yang, X.; Burnette, B.; Arina, A.; Li, X. D.; Mauceri, H.; Beckett, M.; Darga, T. STING-dependent cytosolic DNA sensing promotes radiation-induced type I interferon-dependent antitumor immunity in immunogenic tumors. *Immunity* 2014;41:843-852, <http://doi:10.1016/j.immuni.2014.10.019>
38. Chandrasekaran S, King MR. Microenvironment of tumor-draining lymph nodes: opportunities for liposome-based targeted therapy. *Int J Mol Sci.* 2014;15(11):20209-20239. <http://doi:10.3390/ijms151120209>
39. Leliefeld PH, Koenderman L, Pillay J. How Neutrophils Shape Adaptive Immune Responses. *Front Immunol.* 2015;6:471. <http://doi:10.3389/fimmu.2015.00471>
40. Spitzer MH, Carmi Y, Reticker-Flynn NE, Kwek SS, Madhiredy D, Martins MM, Gherardini PF, Prestwood TR, Chabon J, Bendall SC, Fong L, Nolan GP, Engleman EG. Systemic Immunity Is Required for Effective Cancer Immunotherapy. *Cell.* 2017;26;168(3), 487-502.e15. <http://doi:10.1016/j.cell.2016.12.022>.
41. Valentina Pucino, David H Gardner, Benjamin A Fisher; Rationale for CD40 pathway blockade in autoimmune rheumatic disorders. *The Lancet Rheumatology* 2020, 2, 5 292-301 [http://doi:10.1016/S2665-9913\(20\)30038-2](http://doi:10.1016/S2665-9913(20)30038-2)
42. Kaneko K, Osada T, Morse MA, et al. Heat shock protein 90-targeted photodynamic therapy enables treatment of subcutaneous and visceral tumors. *Commun Biol.* 2020;3(1):226. <http://doi:10.1038/s42003-020-0956-7>
43. Murphy TL, Murphy KM. Dendritic cells in cancer immunology. *Cell Mol Immunol.* 2022;19(1):3-13. <http://doi:10.1038/s41423-021-00741-5>
44. Alzeibak R, Mishchenko TA, Shilyagina NY, Balalaeva IV, Vedunova MV, Krysko DV. Targeting immunogenic cancer cell death by photodynamic therapy: past, present and future [published correction appears in *J Immunother Cancer.* 2021 Oct;9(10):]. *J Immunother Cancer.* 2021;9(1):e001926. <http://doi:10.1136/jitc-2020-001926>
45. Turubanova VD, Balalaeva IV, Mishchenko TA, et al. Immunogenic cell death induced by a new photodynamic therapy based on photosens and photodithazine. *J Immunother Cancer.* 2019;7(1):350. <http://doi:10.1186/s40425-019-0826-3>
46. Tanaka M, Kataoka H, Yano S, et al. Immunogenic cell death due to a new photodynamic therapy (PDT) with glycoconjugated chlorin (G-chlorin). *Oncotarget.* 2016;7(30):47242-47251. <http://doi:10.18632/oncotarget.9725>
47. Zitvogel L, Casares N, Péquignot MO, Chaput N, Albert ML, Kroemer G. Immune response against dying tumor cells. *Adv Immunol.* 2004;84:131-179. [http://doi:10.1016/S0065-2776\(04\)84004-5](http://doi:10.1016/S0065-2776(04)84004-5)
48. Melcher A, Gough M, Todryk S, Vile R. Apoptosis or necrosis for tumor immunotherapy: what's in a name?. *J Mol Med (Berl).* 1999;77(12):824-833. <http://doi:10.1007/s001099900066>
49. Liu Y, Cao X. The origin and function of tumor-associated macrophages. *Cell Mol Immunol.* 2015;12(1):1-4. <http://doi:10.1038/cmi.2014.83>
50. Chulpanova DS, Kitaeva KV, Rutland CS, Rizvanov AA, Solovyeva VV. Mouse Tumor Models for Advanced Cancer Immunotherapy. *Int J Mol Sci.* 2020;21(11):4118. <http://doi:10.3390/ijms21114118>

51. Beltrán Hernández I, Yu Y, Ossendorp F, Korbelik M, Oliveira S. Preclinical and Clinical Evidence of Immune Responses Triggered in Oncologic Photodynamic Therapy: Clinical Recommendations. *J Clin Med.* 2020;9(2):333. [http:// doi:10.3390/jcm9020333](http://doi:10.3390/jcm9020333)
52. Lemos H, Ou R, McCardle C, et al. Overcoming resistance to STING agonist therapy to incite durable protective antitumor immunity. *J Immunother Cancer.* 2020;8(2):e001182. [http:// doi:10.1136/jitc-2020-001182](http://doi:10.1136/jitc-2020-001182)
53. Schacht V., Szeimies R.-M., Abels C. Photodynamic therapy with 5-aminolevulinic acid induces distinct microcirculatory effects following systemic or topical application. *Photochem. Photobiol. Sci.* 2006;5:452-458. [http:// doi:10.1039/b514128a](http://doi:10.1039/b514128a).
54. Qiang YG, Yow CM, Huang Z. Combination of photodynamic therapy and immunomodulation: current status and future trends. *Med Res Rev.* 2008;28(4):632-644. [http:// doi:10.1002/med.20121](http://doi:10.1002/med.20121)
55. Hwang, H.S., Shin, H., Han, J. et al. Combination of photodynamic therapy (PDT) and anti-tumor immunity in cancer therapy. *Journal of Pharmaceutical Investigation* 48, 143-151 (2018). [http:// doi:10.1007/s40005-017-0377-x](http://doi:10.1007/s40005-017-0377-x)
56. Hao Y, Chung CK, Yu Z, et al. Combinatorial Therapeutic Approaches with Nanomaterial-Based Photodynamic Cancer Therapy. *Pharmaceutics.* 2022;14(1):120. [http:// doi:10.3390/pharmaceutics14010120](http://doi:10.3390/pharmaceutics14010120)
57. Huis In 't Veld RV, Da Silva CG, Jager MJ, Cruz LJ, Ossendorp F. Combining Photodynamic Therapy with Immunostimulatory Nanoparticles Elicits Effective Anti-Tumor Immune Responses in Preclinical Murine Models. *Pharmaceutics.* 2021;13(9):1470. [http:// doi:10.3390/pharmaceutics13091470](http://doi:10.3390/pharmaceutics13091470)
58. Foote JB, Kok M, Leatherman JM, et al. A STING Agonist Given with OX40 Receptor and PD-L1 Modulators Primes Immunity and Reduces Tumor Growth in Tolerized Mice. *Cancer Immunol Res.* 2017;5(6):468-479. [http:// doi:10.1158/2326-6066.CIR-16-0284](http://doi:10.1158/2326-6066.CIR-16-0284)
59. Jin F, Liu D, Xu X, Ji J, Du Y. Nanomaterials-Based Photodynamic Therapy with Combined Treatment Improves Antitumor Efficacy Through Boosting Immunogenic Cell Death. *Int J Nanomedicine.* 2021;16:4693-4712. [http:// doi:10.2147/IJN.S314506](http://doi:10.2147/IJN.S314506)
60. Spriggs MK, Armitage RJ, Strockbine L, et al. Recombinant human CD40 ligand stimulates B cell proliferation and immunoglobulin E secretion. *J Exp Med.* 1992;176(6):1543-1550. [http:// doi:10.1084/jem.176.6.1543](http://doi:10.1084/jem.176.6.1543)
61. Kondo E, Gryschock L, Klein-Gonzalez N, et al. CD40-activated B cells can be generated in high number and purity in cancer patients: analysis of immunogenicity and homing potential. *Clin Exp Immunol.* 2009;155(2):249-256. [http:// doi:10.1111/j.1365-2249.2008.03820.x](http://doi:10.1111/j.1365-2249.2008.03820.x)
62. Koike T, Harada K, Horiuchi S, Kitamura D. The quantity of CD40 signaling determines the differentiation of B cells into functionally distinct memory cell subsets. *Elife.* 2019;8:e44245. [http:// doi:10.7554/eLife.44245](http://doi:10.7554/eLife.44245)
63. Wherry EJ, Teichgräber V, Becker TC, et al. Lineage relationship and protective immunity of memory CD8 T cell subsets. *Nat Immunol.* 2003;4(3):225-234. [http:// doi:10.1038/ni889](http://doi:10.1038/ni889)
64. Martin MD, Badovinac VP. Defining Memory CD8 T Cell. *Front Immunol.* 2018;9:2692. [http:// doi:10.3389/fimmu.2018.02692](http://doi:10.3389/fimmu.2018.02692)
65. Meng Z, Zhou X, Xu J, et al. Light-Triggered In Situ Gelation to Enable Robust Photodynamic-Immunotherapy by Repeated Stimulations. *Adv Mater.* 2019;31(24):e1900927. [http:// doi:10.1002/adma.201900927](http://doi:10.1002/adma.201900927)
66. Alvarez M, Molina C, De Andrea CE, et al. Intratumoral co-injection of the poly I:C-derivative BO-112 and a STING agonist synergize to achieve local and distant anti-tumor efficacy. *J Immunother Cancer.* 2021;9(11):e002953. [http:// doi:10.1136/jitc-2021-002953](http://doi:10.1136/jitc-2021-002953)

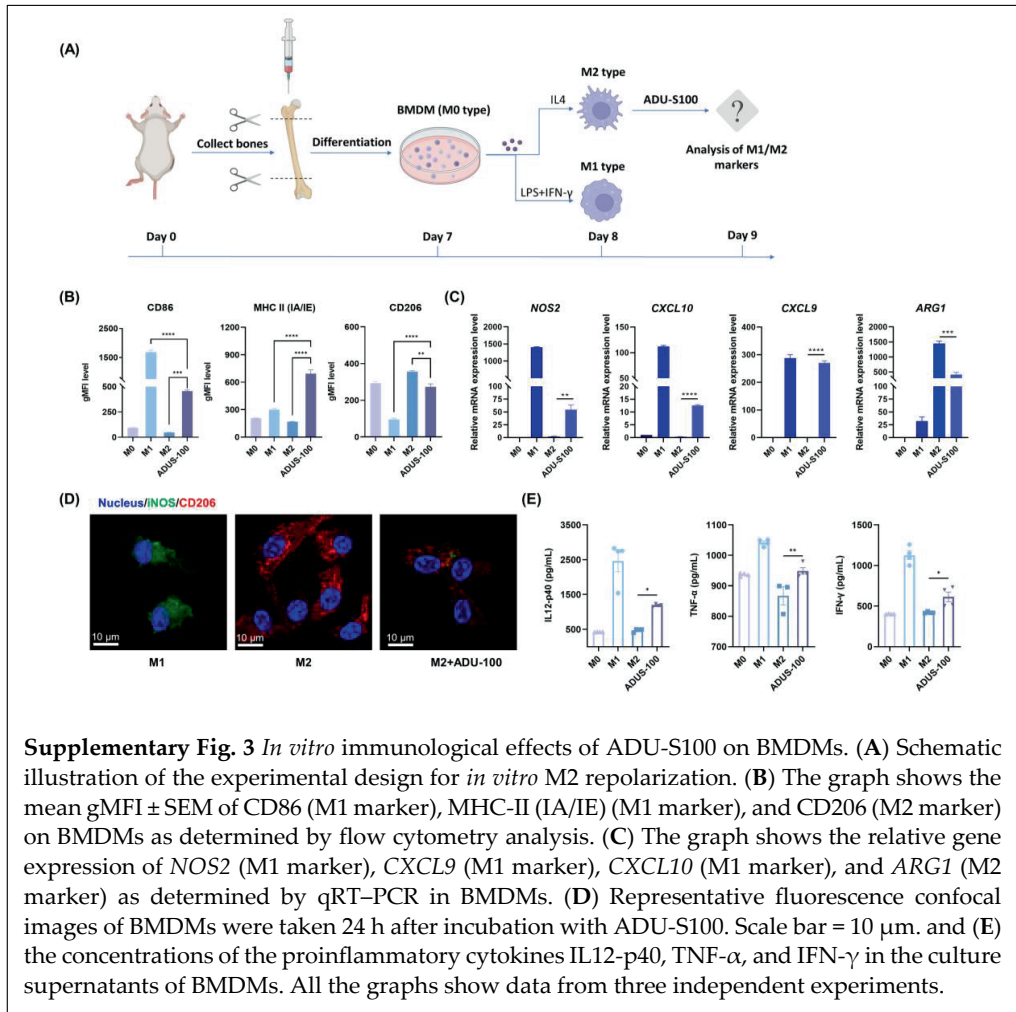
Supporting Information



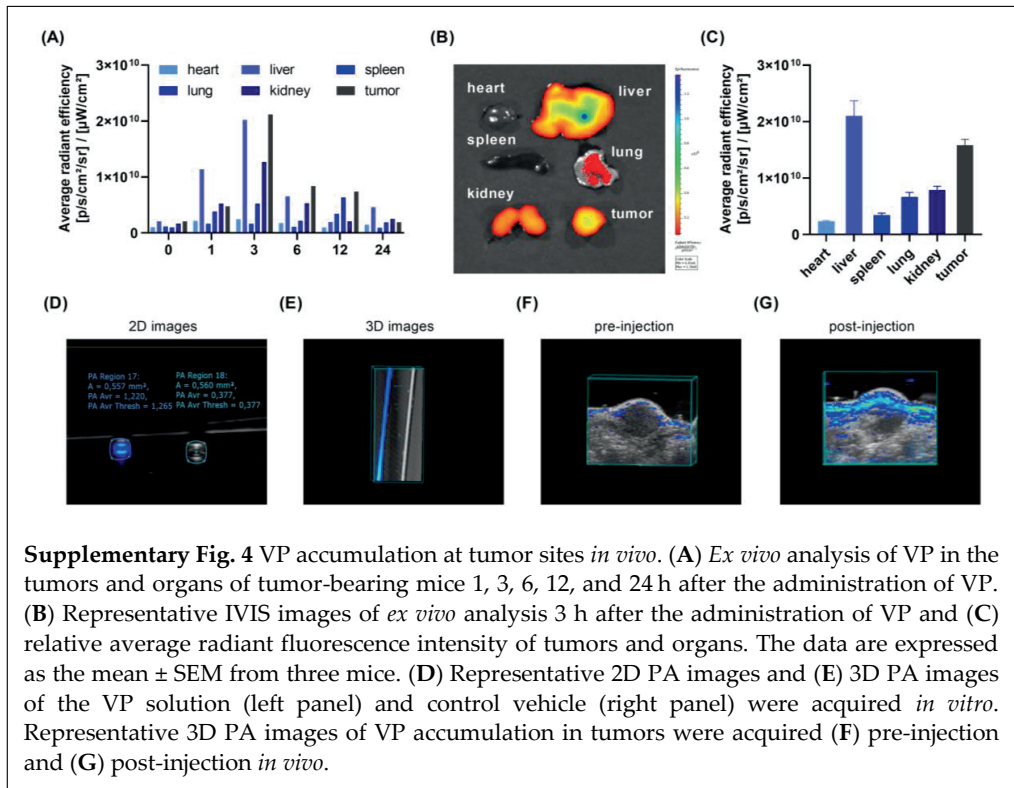
Supplementary Fig. 1 VP characterization and PDT effects *in vitro*. **(A)** Standard curves for NIR signal intensity were generated at 700 nm. **(B)** VP levels in tumor cells were determined by measuring the NIR fluorescence signal intensity of each well at 700 nm. The data are expressed as the means \pm SEMs. **(C)** Retention assay with $0.5 \mu\text{mol/L}$ VP and MC38 cells. The graphs show the relative gMFI compared with the samples of the 0 h group. **(D)** Retention assay with $0.5 \mu\text{mol/L}$ VP and MC38 cells. The graphs show the relative gMFI compared with the samples of the 0 h group. **(E)** ROS generated in MC38 cells and **(F)** CT26 cells after VP-mediated PDT. The graphs show fold changes in gMFI (DCFH-DA) in tumor cells after exposure to various VP concentrations. The horizontal axis represents the VP concentration used. **(G)** The effects of time intervals between VP incubation and laser irradiation on phototoxicity in MC38 cells and **(H)** CT26 cells. The graphs show the percentages of Annexin V-positive cells at each time point. The horizontal axis represents the time intervals between VP injection and laser irradiation.

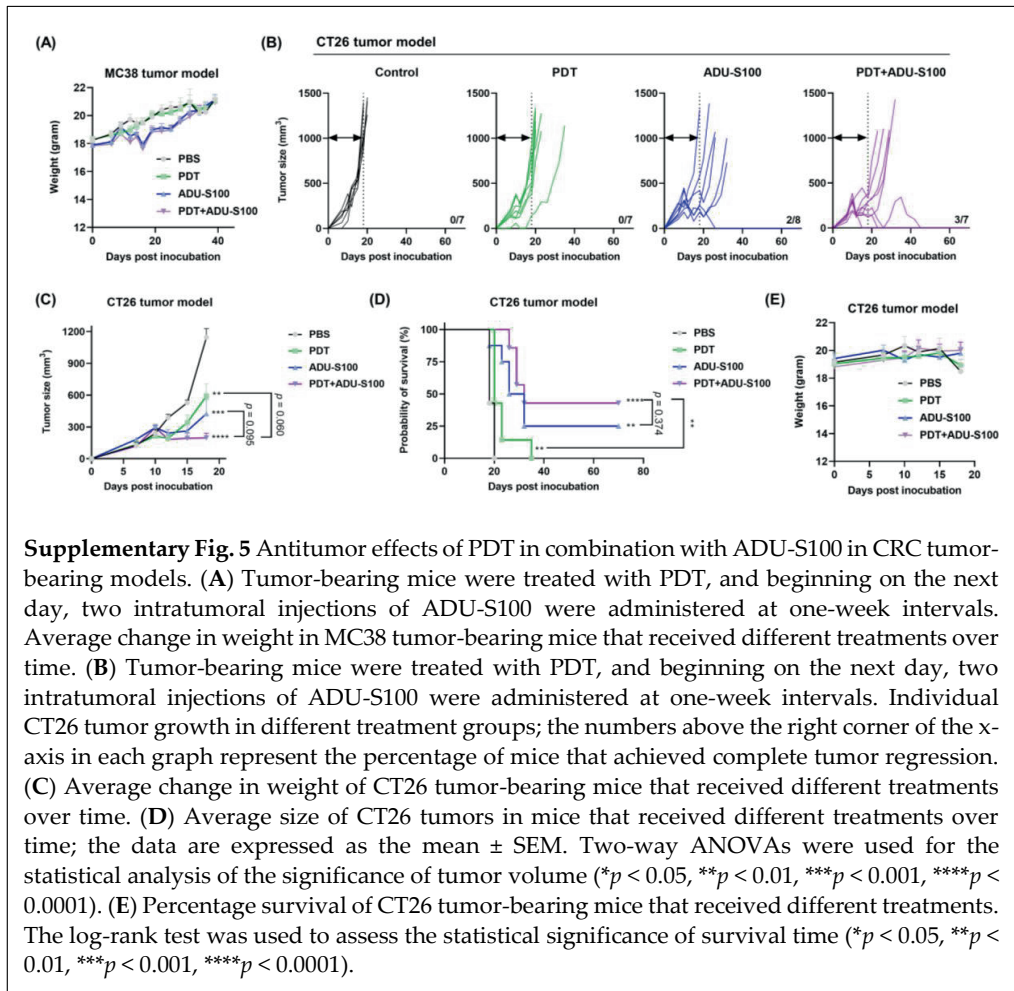


Supplementary Fig. 2 *In vitro* DC activation assay of ADU-S100. The gMFIs of (A) CD40 expression, (B) CD86 expression on DCs (CD11c⁺DAPI⁻ cells), and (C) IL12-p40 secretion in the supernatant were compared to those of the control group of untreated DCs. The data are expressed as the mean values \pm SEMs from three independent experiments and were statistically analyzed by an unpaired two-tailed Student's t test compared to the untreated group (* $p < 0.05$, ** $p < 0.01$, *** $p < 0.001$, **** $p < 0.0001$).

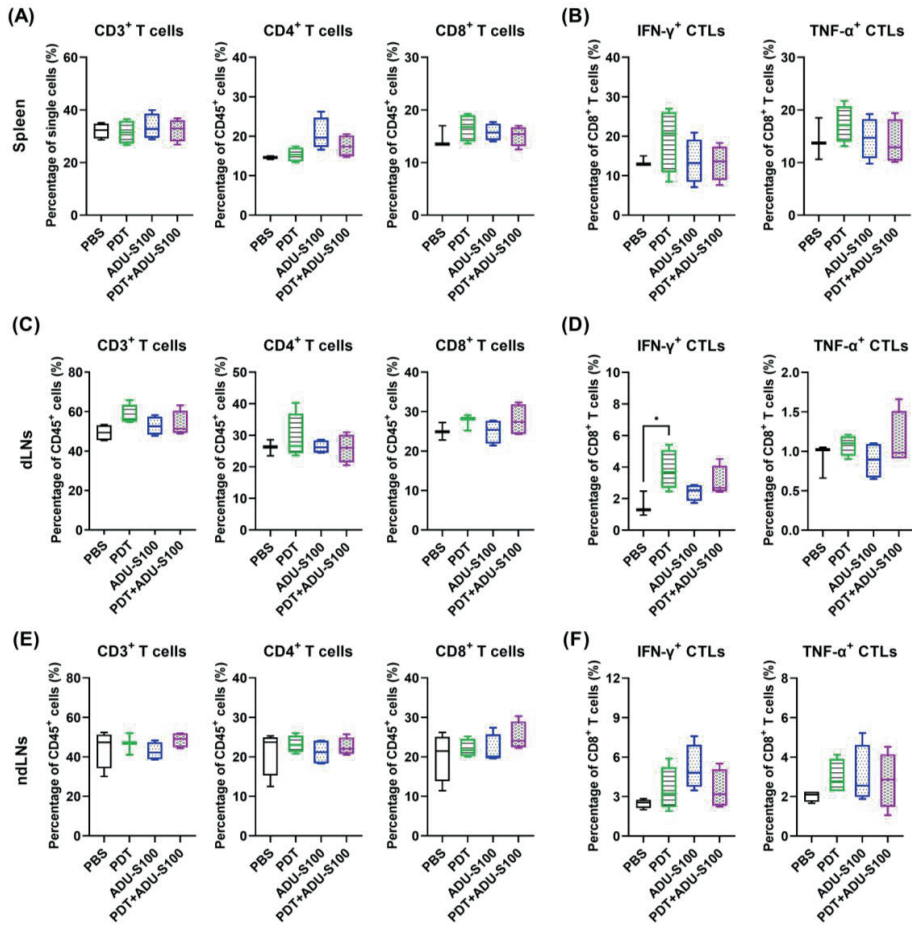


Supplementary Fig. 3 *In vitro* immunological effects of ADU-S100 on BMDMs. **(A)** Schematic illustration of the experimental design for *in vitro* M2 repolarization. **(B)** The graph shows the mean gMFI \pm SEM of CD86 (M1 marker), MHC-II (IA/IE) (M1 marker), and CD206 (M2 marker) on BMDMs as determined by flow cytometry analysis. **(C)** The graph shows the relative gene expression of *NOS2* (M1 marker), *CXCL9* (M1 marker), *CXCL10* (M1 marker), and *ARG1* (M2 marker) as determined by qRT-PCR in BMDMs. **(D)** Representative fluorescence confocal images of BMDMs were taken 24 h after incubation with ADU-S100. Scale bar = 10 μ m. and **(E)** the concentrations of the proinflammatory cytokines IL12-p40, TNF- α , and IFN- γ in the culture supernatants of BMDMs. All the graphs show data from three independent experiments.

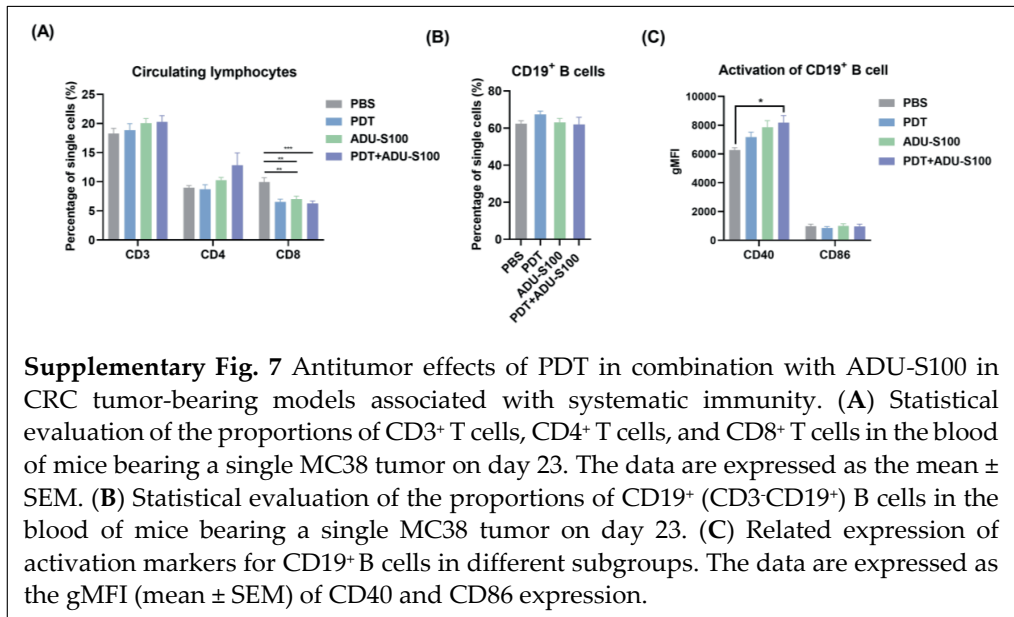


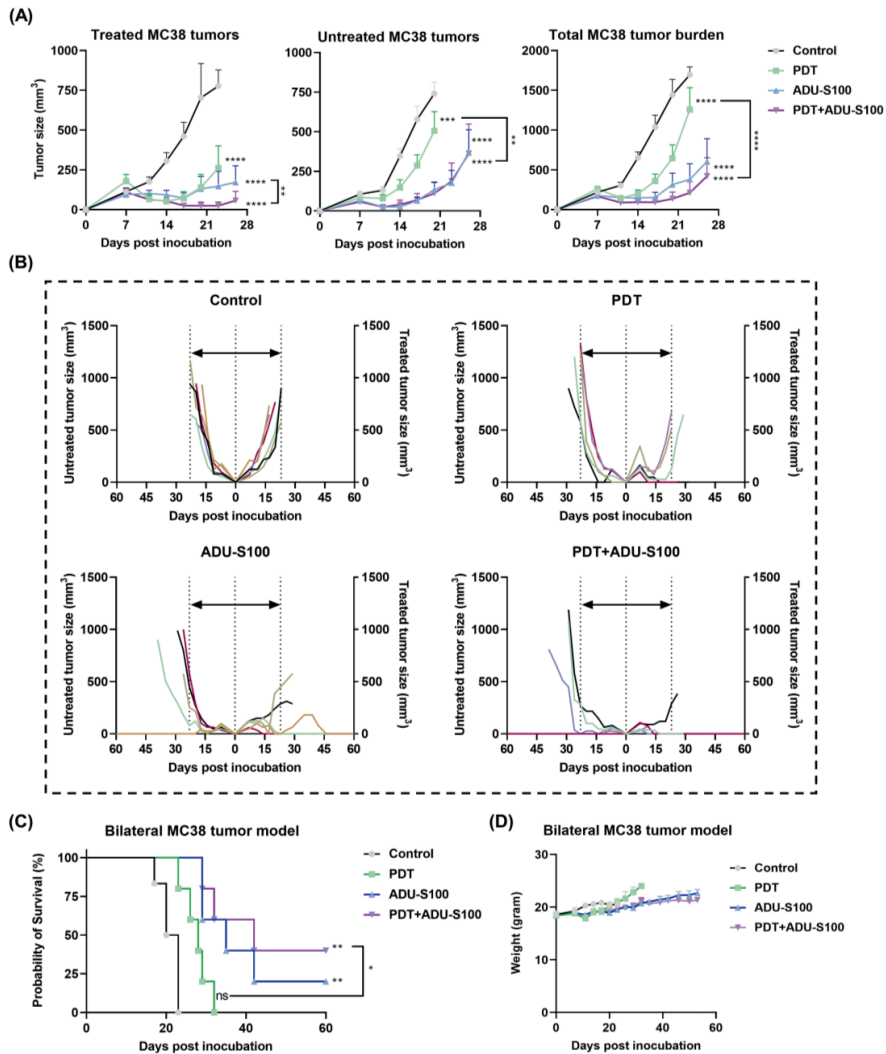


Supplementary Fig. 5 Antitumor effects of PDT in combination with ADU-S100 in CRC tumor-bearing models. **(A)** Tumor-bearing mice were treated with PDT, and beginning on the next day, two intratumoral injections of ADU-S100 were administered at one-week intervals. Average change in weight in MC38 tumor-bearing mice that received different treatments over time. **(B)** Tumor-bearing mice were treated with PDT, and beginning on the next day, two intratumoral injections of ADU-S100 were administered at one-week intervals. Individual CT26 tumor growth in different treatment groups; the numbers above the right corner of the x-axis in each graph represent the percentage of mice that achieved complete tumor regression. **(C)** Average change in weight of CT26 tumor-bearing mice that received different treatments over time. **(D)** Average size of CT26 tumors in mice that received different treatments over time; the data are expressed as the mean \pm SEM. Two-way ANOVAs were used for the statistical analysis of the significance of tumor volume (* $p < 0.05$, ** $p < 0.01$, *** $p < 0.001$, **** $p < 0.0001$). **(E)** Percentage survival of CT26 tumor-bearing mice that received different treatments. The log-rank test was used to assess the statistical significance of survival time (* $p < 0.05$, ** $p < 0.01$, *** $p < 0.001$, **** $p < 0.0001$).

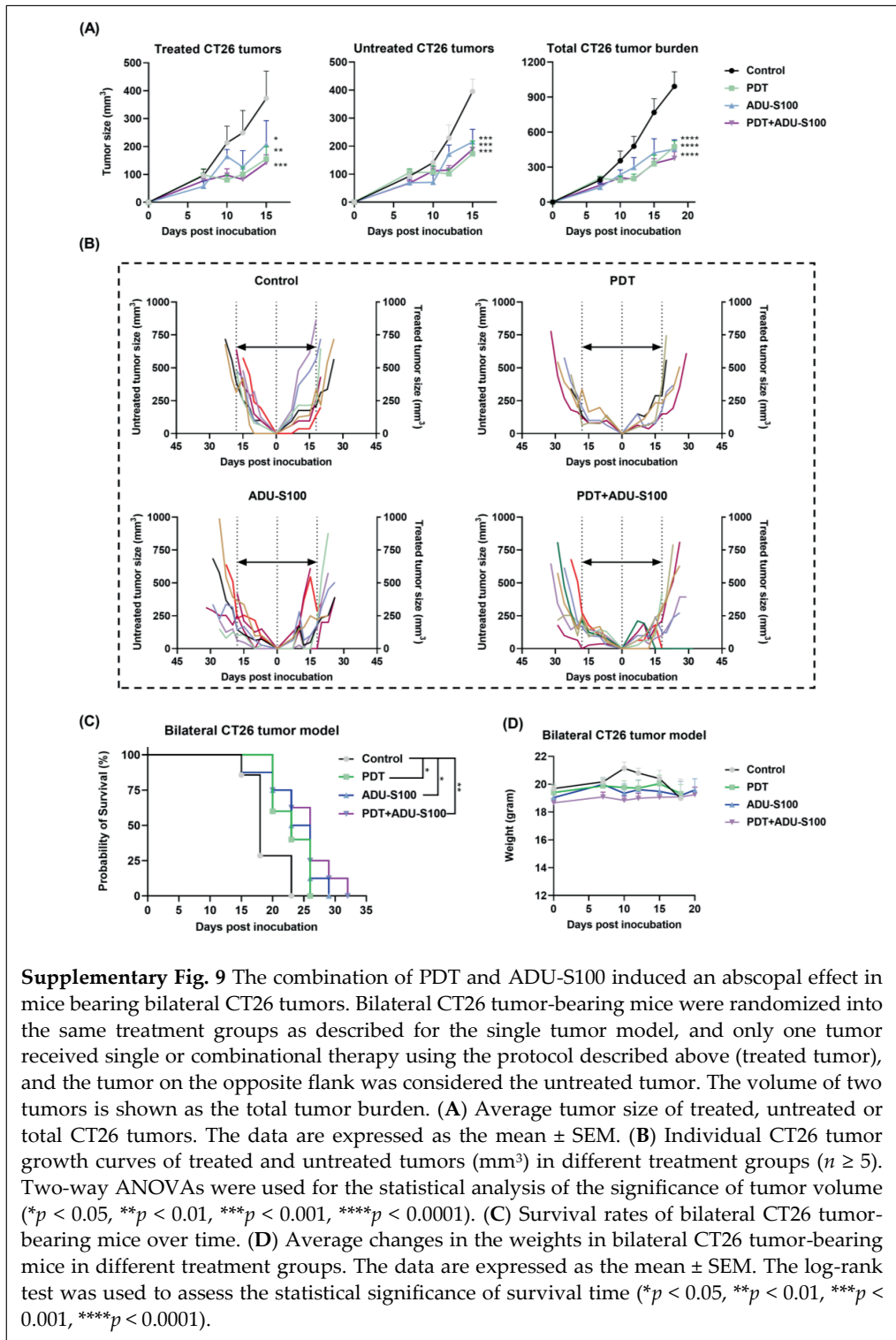


Supplementary Fig. 6 Changes in the immune cell populations in the lymph nodes and spleen after treatment with the combination of PDT and ADU-S100. The percentages of (A) CD3⁺ T cells, CD3⁺ CD4⁺ T cells, and CD3⁺CD8⁺ T cells in the spleen of mice that received different treatments. Live (DAPI) CD45⁺ cells were further gated to identify CD3⁺ T cells, CD4⁺ T cells (CD3⁺CD4⁺), and CD8⁺ T cells (CD3⁺CD8⁺). (B) Splenic CD3⁺CD8⁺ cells were further gated to identify IFN- γ -positive CTLs and TNF- α -positive CTLs. (C) CD3⁺ T cells, CD3⁺ CD4⁺ T cells, and CD3⁺CD8⁺ T cells in the dLNs of mice that received different treatments. (D) CD3⁺CD8⁺ T cells in dLNs were further gated to identify IFN- γ -positive CTLs and TNF- α -positive CTLs. (E) CD3⁺ T cells, CD3⁺ CD4⁺ T cells, and CD3⁺CD8⁺ T cells in the nontumor draining lymph nodes (ndLNs) of mice that received different treatments. (F) CD3⁺CD8⁺ T lymphocytes in ndLNs were further gated to identify IFN- γ -positive CTLs and TNF- α -positive CTLs. The plotted data are expressed as min to max.





Supplementary Fig. 8 The combination of PDT and ADU-S100 induced an abscopal effect in mice bearing bilateral MC38 tumors. Bilateral MC38 tumor-bearing mice were randomized into the same treatment groups as described for the single tumor model, and only one tumor received single or combination treatment using the same protocol as described above (treated tumor). The tumor on the opposite flank was considered the untreated tumor. The volume of two tumors is shown as the total tumor burden. **(A)** Average tumor size of treated, untreated or total MC38 tumors. The data are expressed as the mean \pm SEM. **(B)** Individual MC38 tumor growth curves of treated and untreated tumors (mm³) in different treatment groups ($n \geq 5$) and **(C)** associated survival rates of bilateral MC38 tumor-bearing mice over time. Two-way ANOVAs were used for the statistical analysis of the significance of tumor volume, and the log-rank test was used to assess the statistical significance of survival time (* $p < 0.05$, ** $p < 0.01$, *** $p < 0.001$, **** $p < 0.0001$). **(D)** Average changes in the weights in bilateral MC38 tumor-bearing mice in different treatment groups. The data are expressed as the mean \pm SEM.



Supplementary Fig. 9 The combination of PDT and ADU-S100 induced an abscopal effect in mice bearing bilateral CT26 tumors. Bilateral CT26 tumor-bearing mice were randomized into the same treatment groups as described for the single tumor model, and only one tumor received single or combinational therapy using the protocol described above (treated tumor), and the tumor on the opposite flank was considered the untreated tumor. The volume of two tumors is shown as the total tumor burden. **(A)** Average tumor size of treated, untreated or total CT26 tumors. The data are expressed as the mean \pm SEM. **(B)** Individual CT26 tumor growth curves of treated and untreated tumors (mm³) in different treatment groups ($n \geq 5$). Two-way ANOVAs were used for the statistical analysis of the significance of tumor volume (* $p < 0.05$, ** $p < 0.01$, *** $p < 0.001$, **** $p < 0.0001$). **(C)** Survival rates of bilateral CT26 tumor-bearing mice over time. **(D)** Average changes in the weights in bilateral CT26 tumor-bearing mice in different treatment groups. The data are expressed as the mean \pm SEM. The log-rank test was used to assess the statistical significance of survival time (* $p < 0.05$, ** $p < 0.01$, *** $p < 0.001$, **** $p < 0.0001$).

